Does Topographic Form Stress Impede Prograde Ocean Currents?

YUE BAI*

Department of Atmospheric and Oceanic Sciences, University of California, Los Angeles, California

YAN WANG

Department of Ocean Science and Center for Ocean Research in Hong Kong and Macau, The Hong Kong University of Science and Technology, Hong Kong, China

ANDREW L. STEWART

Department of Atmospheric and Oceanic Sciences, University of California, Los Angeles, California

ABSTRACT

Topographic form stress (TFS) plays a central role in constraining the transport of the Antarctic Circumpolar Current (ACC), and thus the rate of exchange between the major ocean basins. Topographic form stress generation in the ACC has been linked to the formation of standing Rossby waves, which occur because the current is retrograde (opposing the direction of Rossby wave propagation). However, it is unclear whether TFS similarly retards current systems that are prograde (in the direction of Rossby wave propagation), which cannot arrest Rossby waves. An isopycnal model is used to investigate the momentum balance of wind-driven prograde and retrograde flows in a zonal channel, with bathymetry consisting of either a single ridge or a continental shelf and slope with a meridional excursion. Consistent with previous studies, retrograde flows are almost entirely impeded by TFS, except in the limit of flat bathymetry, whereas prograde flows are typically impeded by a combination of TFS and bottom friction. A barotropic theory for standing waves shows that bottom friction serves to shift the phase of the standing wave's pressure field from that of the bathymetry, which is necessary to produce TFS. The mechanism is the same in prograde and retrograde flows, but is most efficient when the mean flow arrests a Rossby wave with a wavelength comparable to that of the bathymetry. The asymmetry between prograde and retrograde momentum balances implies that prograde current systems may be more sensitive to changes in wind forcing, for example associated with climate shifts.

1. Introduction

The momentum balance of the Antarctic Circumpolar Current (ACC) has been a focus of research in physical oceanography for several decades (Munk and Palmén 1951; Tréguier and McWilliams 1990; Olbers et al. 2004; Howard et al. 2015). The established community understanding is that the eastward flow momentum is sourced primarily from the Southern Hemisphere mid-latitude westerly winds. The mechanism via which this momentum is transferred to the sea floor dictates, in part, the response of the ACC to changes in the winds (Munk and Palmén 1951; Straub 1993; Abernathey and Cessi 2014), with implications for global transports of water masses and tracers between ocean basins (*e.g.* Talley 2013; Thompson et al. 2016). Understanding this response is particularly relevant in light of the multi-decadal trends in the Southern Annular Mode (Marshall 2003; Hazel and Stewart 2019).

Munk and Palmén (1951) first proposed that topographic form stress, *i.e.* pressure gradients acting zonally across zonal variations in the sea floor elevation, must be the primary sink of eastward momentum in the ACC. It has subsequently been proposed that the surface wind source and sea floor sink of momentum are connected by a sustained downward momentum flux via isopycnal form stress, owing to a combination of transient and standing eddies (Johnson and Bryden 1989; Tréguier and McWilliams 1990; Warren et al. 1996; Hughes 1997; Olbers 1998). Various model studies have subsequently confirmed these predictions (Stevens and Ivchenko 1997; Ward and Hogg 2011; Stewart and Hogg 2017). Though difficult to evaluate directly using observations, analysis of the Southern Ocean State Estimate (Mazloff et al. 2010) confirms that topographic form stress balances approximately 95% of the wind-input zonal momentum (Masich et al. 2015). Furthermore, isopycnal form stresses associated with the time-mean flow are the primary agent via which that momentum is transferred from the surface to the sea floor (Masich et al. 2018).

The establishment of topographic form stresses in the ACC has been linked to the presence of standing Rossby waves, or "standing meanders" (Thompson and Naveira Garabato 2014; Youngs et al. 2017; Langlais et al.

*Corresponding author: Yue Bai, baiyue@ucla.edu

2017). These structures arise due to the opposing directions of the mean flow and Rossby wave propagation (Marshall 1995, 2016), and are associated with elevated mesoscale eddy genesis and energy (Bischoff and Thompson 2014; Thompson and Naveira Garabato 2014; Youngs et al. 2017; Stanley et al. 2020), and subduction of dissolved gases (Langlais et al. 2017). Adjustments of these standing wave structures have been proposed to balance temporal fluctuations in the zonal-mean wind stress over the Southern Ocean (*e.g.* Thompson and Naveira Garabato 2014). The topographic form stress has been shown to adjust to changes in the wind stress on much shorter time scales than the isopycnal form stress (Ward and Hogg 2011), consistent with a barotropic Rossby wave adjustment process. Other idealized studies have suggested that for sufficiently strong winds, closed, gyre-like recirculations form in an ACC-like channel, and further increases in the wind stress are balanced by changes in the gyre circulations, rather than the standing meanders (Nadeau and Ferrari 2015; Stewart and Hogg 2017). In addition, the intrinsic speed of Rossby wave propagation relative to the mean flow speed has been shown to determine the occurrence of shear instabilities (Arnol'd 1966). This has recently been characterized in retrograde flows via the "Mach number" (Stanley et al. 2020).

However, a similar level of understanding has been lacking in current systems in which the direction of Rossby wave propagation matches that of the mean currents. Such current systems are referred as "prograde", in contrast to the "retrograde" mean flow of the ACC. In such systems, one might expect arrest of Rossby waves by the mean flow to be suppressed, and thus it is unclear whether topographic form stress should continue to dominate the momentum budget. In fact, in Section 4 we will show that standing waves exist and support topographic form stress in both prograde and retrograde currents. In nature these current systems often occur over continental slopes, where the relevant wave propagation speed is that of topographic Rossby waves. Prominent examples include the Antarctic Slope Current (Jacobs 1991; Thompson et al. 2018), the East and West Greenland Currents (Brearley et al. 2012; Myers et al. 2009), and the Norwegian Atlantic Current (Gascard et al. 2004). Similar to the ACC, the mechanism via which wind-input momentum is balanced in these current systems has direct implications for the sensitivity of their along- and across-slope exchanges to changes in the atmospheric circulation (*e.g.* Stewart and Thompson 2012; Spall and Thomas 2016; Stewart and Thompson 2015a; Schulze Chretien and Frajka-Williams 2018; Stewart et al. 2018; Goszczko et al. 2018).

There have been relatively few previous investigations of the momentum balance in prograde current systems. Brink (1986) showed that barotropic flows over continental shelves incur asymmetric topographic stresses depending on their orientation relative to the direction of coastal wave propagation. Similarly, alongshore variations in continental shelf bathymetry induce flow adjustments only the "down-wave" direction, *i.e.* in the direction of shelf wave propagation (Pringle 2002). Recent studies have investigated the specific momentum balance of the Antarctic Slope Current, but have either excluded along-shore bathymetric variations (Stewart and Thompson 2013, 2016) or have been unable to unambiguously characterize the mechanisms of momentum extraction from the current (Stewart et al. 2019). Consqeuently, a comprehensive theoretical understanding of the momentum balance in prograde current systems is yet to be established.

In this article, we use an idealized isopycnal channel model to investigate the extraction of wind-input momentum from prograde current systems. In Section 2 we describe the model physics and our experimental configuration. In Section 3 we contrast the circulation patterns and momentum balances of reference simulations forced by prograde and retrograde winds (Section 3a). We then investigate the physical controls on the circulation and the momentum balance via a series of perturbation experiments with varying bathymetric elevations (Section 3b), surface wind stresses and bottom frictions (Section 3c). In Section 4 we develop a quasigeostrophic, barotropic theory for wind-forced standing waves to facilitate interpretation of our experimental results, and compare the theoretical predictions against our numerical model diagnostics. Motivated by the specific examples of prograde slope currents given above, in Section 5 we extend our experiments and theory to the momentum balance over a continental shelf/slope-like bathymetry. In Section 6 we discuss our results and provide concluding remarks.

2. Model configuration

We idealize the dynamics of the ACC as a wind-driven baroclinic flow in a rectilinear channel, similar to the approach taken in various previous studies (*e.g.* Hallberg and Gnanadesikan 2001; Abernathey et al. 2011; Stewart and Thompson 2013; Howard et al. 2015; Patmore et al. 2019). Specifically, we define a zonally re-entrant channel bounded meridionally by vertical walls. The meridional width of the channel is $L_y = 2000\,\mathrm{km}$, which approximately matches the width of the ACC, while the zonal length $L_x = 2000\,\mathrm{km}$ has been chosen to minimize both flow self-interaction due to the zonal periodic boundary condition and computational cost (simulations with $L_x = 4000\,\mathrm{km}$ show no qualitative difference). To allow the flow to develop topographic form stress, we include a simple meridional ridge across the center of the channel. Specifically, we prescribe the bathymetry $z = \eta_b(x, y)$ as

$$\eta_b(x) = -H + H_\mathrm{b} \exp\left[-\left(\frac{x - X_\mathrm{b}}{\frac{1}{2} W_\mathrm{b}} \right)^2 \right]. \qquad (1)$$

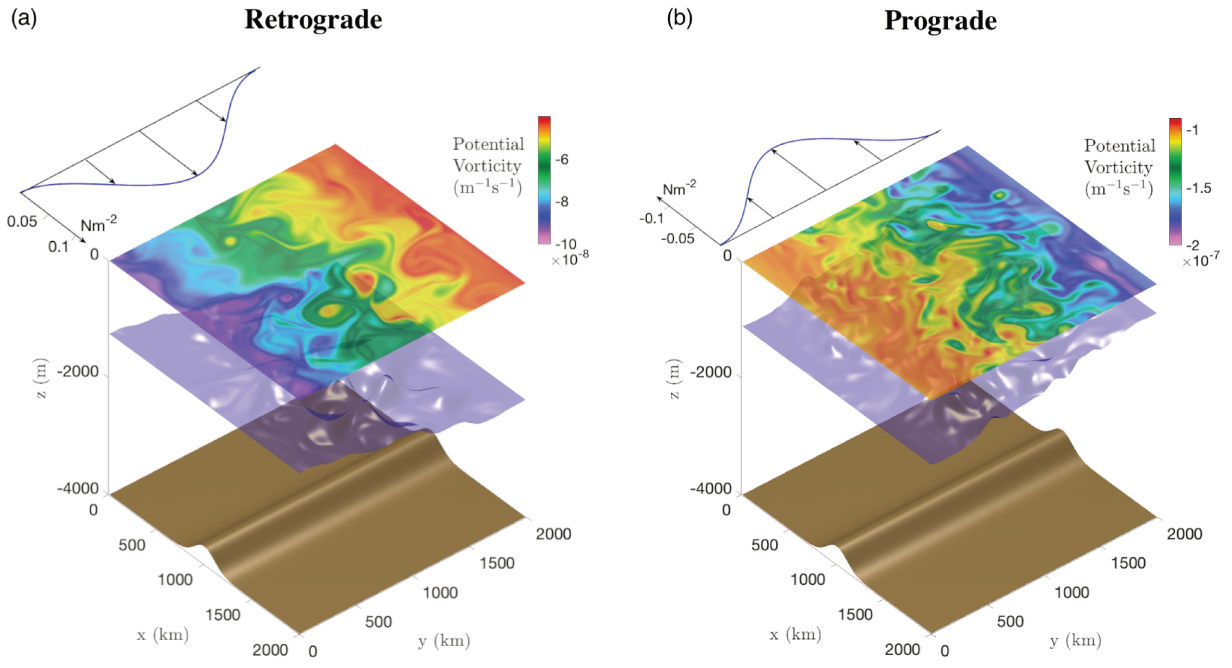

FIG. 1. Configuration of our isopycnal channel model. 3D renderings of snapshots of our (left) retrograde and (right) prograde reference simulations (see Sec. 2), showing the surface wind stress (blue curve), the bathymetry (brown), the interface between the two isopycnal layers (blue), and the upper-layer potential vorticity (color scale).

The channel is posed on a southern hemisphere mid-latitude β-plane, with Coriolis parameter $f = f_0 + \beta(y - L_y/2)$, $f_0 = -1\times10^{-4}\,\mathrm{s}^{-1}$ and $\beta = 1.5\times10^{-11}\,\mathrm{m}^{-1}\,\mathrm{s}^{-1}$. The model geometry is illustrated in Fig. 1, and key parameters are listed in Table 1.

We idealize the ACC's baroclinic structure by discretizing the vertical stratification into two isopycnal layers, the minimum required to permit the development of baroclinic instabilities that sustain the ACC's eddy field (Hallberg and Gnanadesikan 2001; Thompson 2008; Jansen et al. 2015; Meredith 2016). The dynamics are governed by the momentum equation,

$$\frac{\partial \boldsymbol{u}_k}{\partial t} + h_k q_k \hat{\boldsymbol{z}}\times\boldsymbol{u}_k + \nabla\left(M_k + \tfrac{1}{2}\boldsymbol{u}_k^2\right) = \delta_{1,k}\frac{\tau}{\rho_0 h_1}\hat{\boldsymbol{x}} - \delta_{2,k}\frac{C_\mathrm{d}}{h_2}|\boldsymbol{u}_2|\boldsymbol{u}_2 + \frac{1}{h_k}\nabla\cdot\boldsymbol{\sigma}_k, \quad (2)$$

and volume conservation,

$$\frac{\partial h_k}{\partial t} + \nabla\cdot(h_k\boldsymbol{u}_k) = 0, \quad (3)$$

where $k = 1$ denotes the upper layer and $k = 2$ denotes the lower layer. Here we denote the horizontal velocities as $\boldsymbol{u}_k$ and the layer thicknesses as h_k, with $\hat{\boldsymbol{x}}$ and $\hat{\boldsymbol{z}}$ being dimensionless unit vectors. We additionally introduce the potential vorticity,

$$q_k = \frac{f_0 + \beta y + \zeta_k}{h_k}, \quad (4)$$

and the Montgomery potential,

$$M_k = \pi - \delta_{2,k}\, g' h_1. \quad (5)$$

We make the rigid lid approximation (*e.g.* Vallis 2006; Pinardi et al. 1995), denoting $\pi = p_\mathrm{surf}/\rho_0$ as the density-normalized surface pressure, where ρ_0 is a constant reference density. We additionally define $g' = g(\rho_2 - \rho_1)/\rho_1 = 1\times10^{-2}\,\mathrm{m\,s}^{-2}$ as the reduced gravity, which yields a baroclinic deformation radius of $L_d = \sqrt{g' h_1 h_2/(h_1+h_2)}/|f| \approx 25\,\mathrm{km}$ that is representative of the ACC (Chelton et al. 1998; Hallberg 2013).

There is no surface buoyancy forcing. The flow is purely forced mechanically by a steady zonal wind stress $\tau(y)$, with a maximum magnitude $\tau_0 = 0.1\,\mathrm{N\,m}^{-2}$, whose profile approximates the mean stress exerted over the Southern Ocean (*e.g.* Large and Yeager 2009). In particular, we prescribe a simple sinusoidal dependence of the wind stress on latitude, ensuring that both the stress and its curl vanish

TABLE 1. List of parameters used in flat-bottom reference run with a meridional ridge. Italics indicate parameters that are independently varied in our sensitivity experiments.

Parameter	Value	Description
L_x	2000 km	Zonal domain size
L_y	2000 km	Meridional domain size
H	4000 m	Maximum ocean depth
Y_w	1000 km	Peak wind stress position
H_b	300 m	*Bottom ridge height*
W_b	300 km	Bottom ridge width
X_b	1000 km	Bottom ridge longitude
ρ_0	1000 kg m^{-3}	Reference density
g	9.81 m s^{-2}	Gravitational constant
g'	10^{-2} m s^{-2}	Reduced gravity
f_0	-1×10^{-4}s^{-1}	Coriolis parameter
β	1.5×10^{-11}s^{-1}m^{-1}	Coriolis parameter gradient
τ_0	0.1 N m^{-2}	*Wind stress maximum*
C_d	2×10^{-3}	*Quadratic drag coefficient*
A_4	9.5×10^9m^{4}s^{-1}	Biharmonic horizontal viscosity
Δ_h	7.8 km	Horizontal grid spacing
Δ_t	412 s	Time step size

at the meridional boundaries,

$$\tau(y) = \tau_0 \sin^2\left(\frac{\pi y}{L_y}\right). \tag{6}$$

This profile is illustrated in Fig. 1. In the lower isopycnal layer the flow is damped by a quadratic bottom friction with drag coefficient $C_d = 2\times10^{-3}$. We also include a scale-selective dissipation operator, $\nabla\cdot\boldsymbol{\sigma}_k$, to remove grid-scale energy and potential enstrophy. This operator is formulated as a thickness-weighted biharmonic viscosity with a Smagorinsky (1963) coefficient of $A_{Smag} = 4$, prescribed following Griffies and Hallberg (2000). Additionally, we found that simulations with retrograde flows would develop momentum fluxes to the northern boundary, energizing Kelvin waves that ultimately destabilized the model via formation of hydraulic jumps (Hogg et al. 2011). We therefore restore the isopycnal interface to a uniform depth at the northern boundary: 2000 m for retrograde flows and 500 m for prograde flows. The restoring rate varies linearly from 7 days^{-1} at $y = L_y$ to zero at $y = L_y - L_r$, where L_r = 100 km. The model is otherwise adiabatic outside of this region. Some previous studies have also found it necessary to implement a similar restoring (*e.g.* Morrison and Hogg 2013; Howard et al. 2015), while others have not (*e.g.* Abernathey and Cessi 2014).

We solve (2)–(5) numerically using the AWSIM model (Stewart and Dellar 2016; Solodoch et al. 2021). We use a uniform horizontal grid of 256^2 points, yielding a grid spacing of approximately 8 km. Experiments performed at higher resolution produced quantitatively similar results. The spatial discretization is essentially that of Arakawa and Lamb (1981), which exactly conserves energy and potential enstrophy in the absence of explicit forcing and dissipation. The time stepping is performed using the third-order Adams-Bashforth scheme (Durran 1991). The surface pressure is determined diagnostically by solving an elliptic equation at the end of each time step, as described by Zhao et al. (2019).

All simulations discussed in the following sections are initialized with a quiescent deep layer, a mean upper layer thickness of H_1 = 1000 m, with a uniform isopycnal slope of 5×10^{-4} that deepens northward (southward) for retrograde (prograde) experiments, and with a corresponding geostrophically-balanced zonal flow in the upper layer. We then superpose a randomly-generated field of geostrophically-balanced eddies in the upper layer, having a root-mean-square energy of 0.01 m s^{-1} and a peak wavelength of 8 deformation radii. The model is then integrated forward in time until it reaches a statistically steady state, based on time series of the total kinetic and potential energies. All diagnostics are then calculated using averages over 10 years of the model evolution in statistically steady state (averaging instead over 20 changes the results by no more than 2%).

3. Momentum balance of prograde vs. retrograde channel flows

We now describe a series of numerical experiments that compare the dynamics and momentum balances of prograde and retrograde channel flows. We first illustrate the contrast between these cases using two representative reference simulations forced by prograde and retrograde wind stresses, but with otherwise identical parameters. We then perform a series of perturbation experiments with varying bathymetric heights to investigate the emergence of topographic form stress. Finally, we perform additional sensitivity experiments with varying wind stress magnitudes and bottom drag coefficients to (1) compare our findings with previous studies, and (2) highlight those experiments' implications for the sensitivity of major ocean current systems to wind forcing. In Appendix A we test the influence of our channel model's discrete representation of the vertical stratification by reproducing key results using the MIT general circulation model (MITgcm, Marshall et al. 1997a,b).

a. Circulation and momentum balance: a reference case

To aid interpretation of our experimental results, we first use a reference model configuration to compare the prograde and retrograde circulations and momentum balances. For this reference configuration we select a topographic height of H_b = 300 m because the results are representative of most of the parameter space explored in this study (see Section 3b). The model parameters otherwise match those given in Table 1. We conduct one reference simulation with a retrograde wind stress ($\tau_0 = 0.1\,\mathrm{N\,m^{-2}}$), and

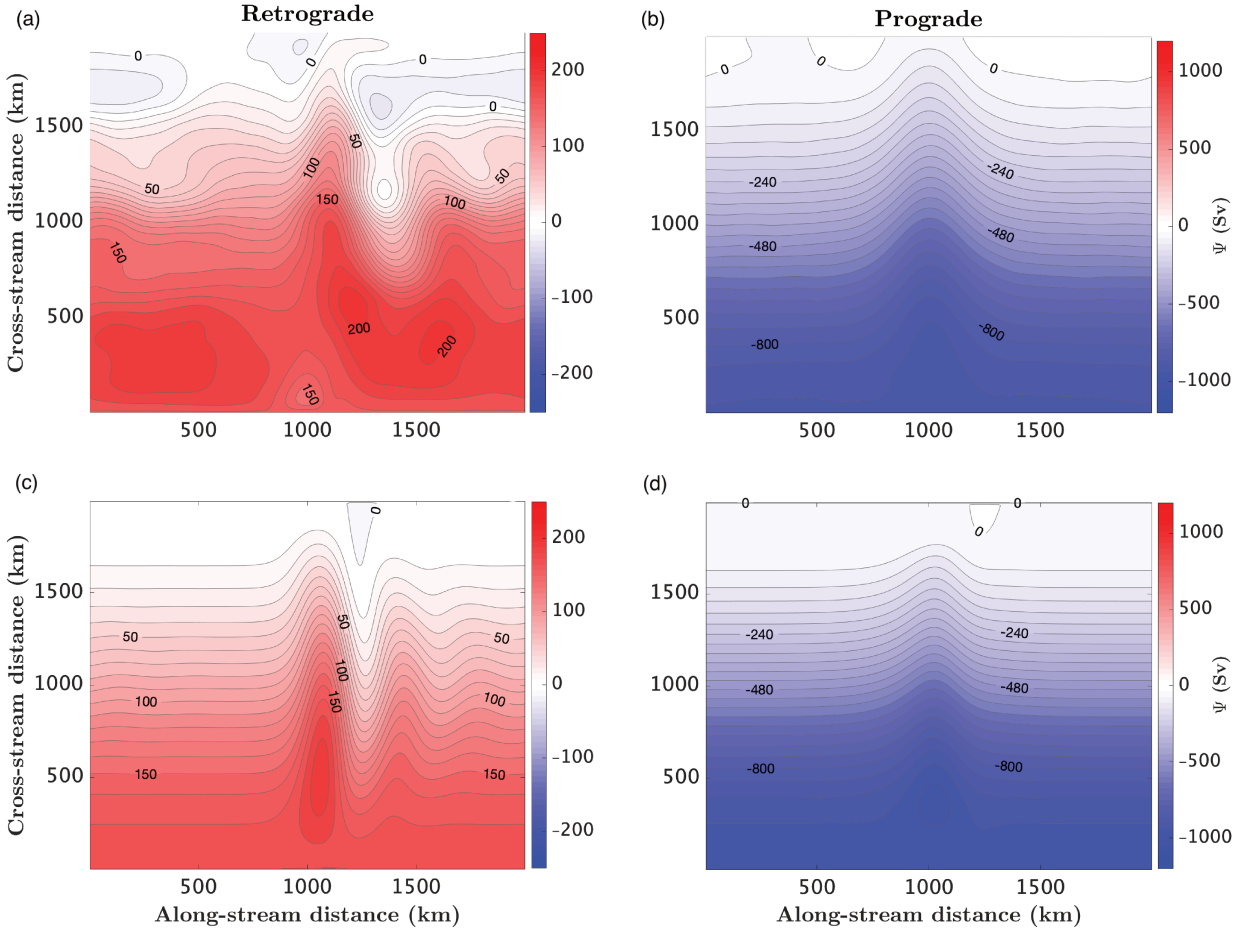

FIG. 2. Depth-integrated streamfunctions in (top panels) our reference retrograde and prograde channel model simulations (Section 3) and (bottom panels) the corresponding predictions of our standing wave theory with an eddy viscosity of $\nu = 1000\,\mathrm{m^2\,s^{-1}}$ (Section 4). The contour interval is 10 Sv in the retrograde case and 40 Sv in the prograde case.

another with a prograde wind stress of the same magnitude ($\tau_0 = -0.1\,\mathrm{N\,m^{-2}}$).

In Figs. 1 and 2 we compare the instantaneous and time-mean circulations that develop in our reference experiments. Isopycnal layers in both directions (the blue layer in Fig. 1) show similar baroclinicity, with a time- and zonally-averaged isopycnal slope of $O(10^{-4})$. The time-mean depth-integrated streamfunctions differ substantially between these experiments (Fig. 2): the retrograde flow develops a distinct standing wave-like pattern in the lee of the ridge, with meridional excursions of individual streamlines on the order of 1000 km. This is consistent with the concept of an arrested wave, as the mean flow speed and the barotropic Rossby wave phase speed are both $O(0.1\,\mathrm{m\,s^{-1}})$. By contrast, baroclinic Rossby wave propagate with a much slower speed of $O(0.01\,\mathrm{m\,s^{-1}})$, assuming a wavelength comparable to the bottom topography. In the prograde experiment, the barotropic streamlines exhibit approximate zonal symmetry about the ridge, suggesting that the flow much more closely adheres to planetary potential vorticity (f/η_b) contours. Snapshots of the instantaneous upper-layer potential vorticity (Fig. 1) indicate that the flow variability also differs substantially between these experiments. In the retrograde case, the eddy field is concentrated in the lee of the ridge, and the largest eddies reach scales of hundreds of kilometers in diameter. By contrast, in the prograde case the eddies are more homogeneously distributed across the model domain, and their diameters are typically only on the order of 100 km.

We now examine how these differences between the prograde and retrograde flow structures reflect differences in their momentum balances. We derive the layer-integrated momentum equation by multiplying (2) by h_k, averaging

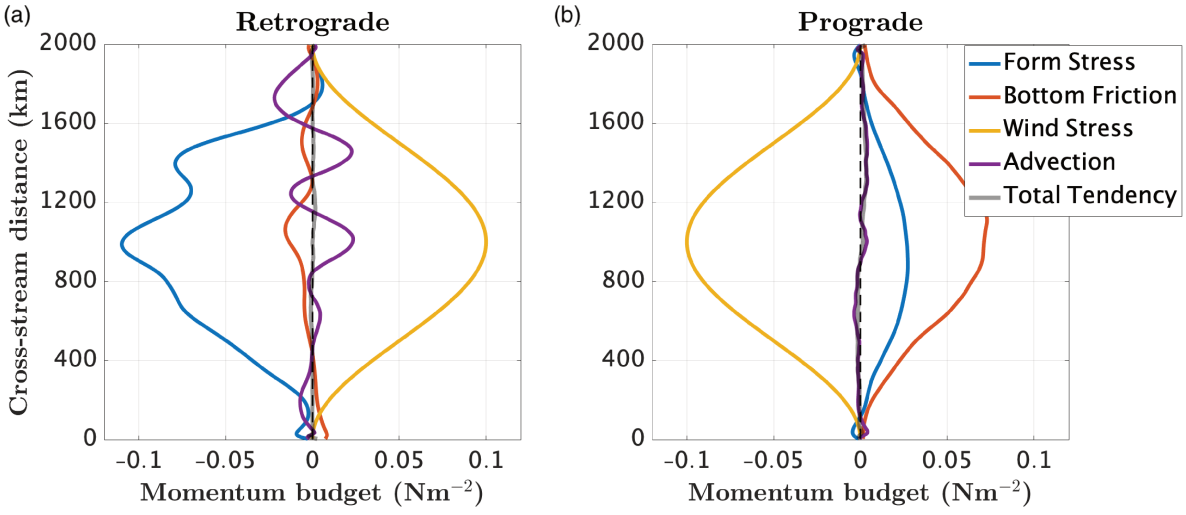

FIG. 3. Zonally and vertically integrated momentum budgets for our (left) retrograde and (right) prograde reference simulations. The curves labeled in the legend correspond to those identified in Eqn. 7. The Total Tendency is the sum of the other four plotted curves, and does not include the viscous stress torque term from Eqn. 7, which is negligible at all latitudes.

zonally and temporally, and summing over the layers:

$$\underbrace{\frac{\partial}{\partial t}\sum_k \overline{h_k u_k}^{x,t}}_{\text{Tendency}} = \underbrace{\frac{\tau}{\rho_0}}_{\text{Wind stress}} \underbrace{-C_\mathrm{d}\overline{|\boldsymbol{u}_2|u_2}^{x,t}}_{\text{Bottom friction}} + \underbrace{\sum_k \left[\overline{h_k^2 q_k v_k}^{x,t} - \overline{h_k \frac{\partial}{\partial x}\left(\tfrac{1}{2}\boldsymbol{u}_k^2\right)}^{x,t} + \overline{u_k \frac{\partial h_k}{\partial t}}^{x,t} \right]}_{\text{Advection}} \underbrace{-\sum_k \overline{h_k \frac{\partial M_k}{\partial x}}^{x,t}}_{\text{Topographic form stress}} + \underbrace{\sum_k \nabla\cdot\overline{\boldsymbol{\sigma}_k^{(x)}}^{x,t}}_{\text{Viscous stress torque}} . \quad (7)$$

Here $\overline{\bullet}^{x,t}$ denotes an average in x and t. Note that the topographic form stress term may be exactly re-written in the more familiar form,

$$\mathrm{TFS} = -\rho_0 \sum_k \overline{h_k \frac{\partial M_k}{\partial x}}^{x,t} = \overline{-p_\mathrm{bot}\frac{\partial \eta_b}{\partial x}}^{x,t} , \quad (8)$$

where $p_\mathrm{bot} = \rho_0\,(\pi + g h_1 + (g+g')h_2)$ is the pressure at the sea floor. However, we diagnose this and other terms as written in (7) because this is consistent with the model's discretization of the momentum equations (Stewart and Dellar 2016). Note also that the thickness restoring at the northern boundary (see Section 2) enters (7) implicitly as a diapycnal advection term via the last term in the Advection bracket.

Fig. 3 shows the contributions of terms in (7) in our reference prograde and retrograde experiments. Consistent with previous studies (*e.g.* Howard et al. 2015; Stewart and Hogg 2017), the advection, tendency, and viscous stress torque terms in (7) make only modest contributions to the domain-integrated momentum balance, though locally the advective momentum flux convergence may be as large as or exceed the wind stress in our retrograde experiments. Thus the domain-integrated wind stress is almost exactly balanced by topographic form stress and bottom friction. This balance holds in all of the experiments, whether prograde or retrograde, that are discussed in this study. We therefore frame our results in terms of the following approximate three-term momentum balance

$$0 \approx \overline{\tau}^y + \overline{\mathrm{TFS}}^y + \overline{\mathrm{Friction}}^y , \quad (9)$$

where $\overline{\bullet}^y$ denotes a meridional average.

Fig. 3 also highlights a pronounced asymmetry between the prograde and retrograde momentum budgets. In the retrograde case, topographic form stress almost completely balances the wind stress at all latitudes, and balances more than 90% of the total wind stress input. This is comparable to previous estimates of topographic form stress in the ACC (Masich et al. 2015). Some minor deviations occur due to localized advective convergences and diverences of momentum, and relatively weak, localized contributions from bottom friction. By contrast, the prograde momentum budget is dominated by a balance between the wind stress and bottom friction, with topographic form stress only balancing around 30% of the domain-integrated wind stress. The partitioning of the momentum balance between bottom friction and topographic forms stress is also very uniform with latitude. Thus, these reference experiments suggest that prograde flows may not establish a standing wave in the lee of topographic features, as occurs in retrograde

flows such as the ACC (Thompson and Naveira Garabato 2014). While the establishment of topographic form stress in prograde flows appears to be reduced, the topographic form stress remains non-negligible in the prograde case (Fig. 3). This appears to contradict previously-established studies (see Section 1) indicating that the formation of a large-amplitude standing wave (meandering over a latitudinal lengthscale comparable to the width of the ridge, as in the retrograde experiment shown in Fig. 2(c)) is an essential ingredient for topographic form stresses to occur. In fact, in Section 4 we will show that standing waves do exist in both directions and support the topographic form stress, but they tend to be much larger in amplitude in the retrograde case.

b. Sensitivity to bathymetric elevation

In Section 3a we showed that there are pronounced differences between prograde and retrograde circulations and momentum balances in our idealized channel model. However, these results are derived from a specific experimental configuration whose results might not generalize; in particular, we used a much lower topographic ridge than might be considered typical of the ACC (Masich et al. 2015). In this and the following subsection we therefore examine a series of sensitivity experiments varying the bottom ridge height H_b, surface wind stress τ_0, and bottom quadratic drag coefficient C_d. A key diagnostic is the partitioning of the momentum balance (9) between topographic form stress and bottom friction, which we quantify via the topographic form stress ratio R_TFS,

$$R_\mathrm{TFS} = \left| \frac{\overline{\mathrm{TFS}}^{y}}{\overline{\tau}^{y}} \right|. \tag{10}$$

As the momentum balance is dominated by wind stress, TFS and bottom friction (see Section 3a and (9)), the relative importance of bottom friction is given approximately by $1 - R_\mathrm{TFS}$. To highlight the implications of changes in the momentum balance, we also compute the total channel transport,

$$T = \sum_k \overline{h_k u_k}^{y,t}, \tag{11}$$

where $\overline{\bullet}^{y,t}$ denotes a meridional integral and temporal average (note the difference between the meridional treatments in $\overline{\bullet}^{y,t}$ and $\overline{\bullet}^{y}$ defined above). Note that (11) is insensitive to longitude and so can be computed at any x, due to periodicity and mass conservation. We further decompose T approximately into barotropic and baroclinic components, defining the barotropic transport T_BT using the lower-layer velocity at $x = 0$,

$$T_\mathrm{BT} = \sum_k \overline{h_k u_2}^{y,t}\Big|_{x=0}, \tag{12a}$$

$$T_\mathrm{BC} = T - T_\mathrm{BT}. \tag{12b}$$

We first discuss a series of experiments in which the height of the ridge, H_b, is successively increased from zero to 1000 m in increments of 100 m. These experiments serve to compare the emergence of topographic form stress, starting from the case of a purely flat bathymetry, in which $R_\mathrm{TFS} = 0$ by necessity. Fig. 4 shows that the retrograde wind stress is balanced almost entirely by topographic form stress when the ridge is as low as 200 m. Below $H_\mathrm{b} =$ 200 m, R_TFS decreases sharply to zero, following a similar dependence as found by Tréguier and McWilliams (1990). Qualitatively, this occurs because a smaller ridge requires a larger-amplitude standing meander to produce the same topographic form stress across the ridge (see Thompson and Naveira Garabato 2014). When the ridge becomes sufficiently small, the barotropic flow associated with the meander becomes strong enough to incur non-negligible zonal frictional forces, and thus R_TFS decreases.

In our prograde experiments, the topographic form stress ratio R_TFS exhibits a qualitatively different dependence on H_b from the retrograde experiments. Fig. 4 shows that R_TFS increases steadily as H_b increases from 0 to 1000 m, beyond which $R_\mathrm{TFS} \approx 1$ (not shown). Thus bottom friction plays an important role in the momentum balance over a much larger range of ridge heights in the prograde experiments. This qualitatively supports the expectation described in Section 1, *i.e.* that the inability of prograde flows to support standing Rossby waves should suppress topographic form stress. However, topographic form stress dominates the momentum balance for sufficiently large ridge heights, regardless of the direction of the mean flow relative to planetary wave propagation.

Fig. 4 also shows that the variation of R_TFS with H_b corresponds closely with variations of the zonal transport T. In both the prograde and retrograde cases, the transport is relatively large in the absence of a ridge, reaching approximately 1100 Sv at $H_\mathrm{b} = 0$. This occurs because friction must balance the wind stress in this limit, which requires relatively strong bottom flows, and thus a much larger total transport (Munk and Palmén 1951). As the ridge height increases, the transport decreases, asymptoting to a value of 100–200 Sv that is consistent with observations of the ACC transport (Donohue et al. 2016). In this limit a pressure gradient across the ridge, and thus a topographic form stress, can be established by relatively weak bottom flows, and thus a much lower net transport (Nadeau and Ferrari 2015). However, consistent with Fig. 4, the retrograde experiments approach the low-transport, topographic form stress-dominated regime at a much smaller H_b.

c. Sensitivity to surface wind stress and bottom friction

As seen from the previous subsection, topographic form stress dominates the prograde momentum balance provided that the bottom obstacle is sufficiently prominent. In other words, factors other than bottom elevation might be more

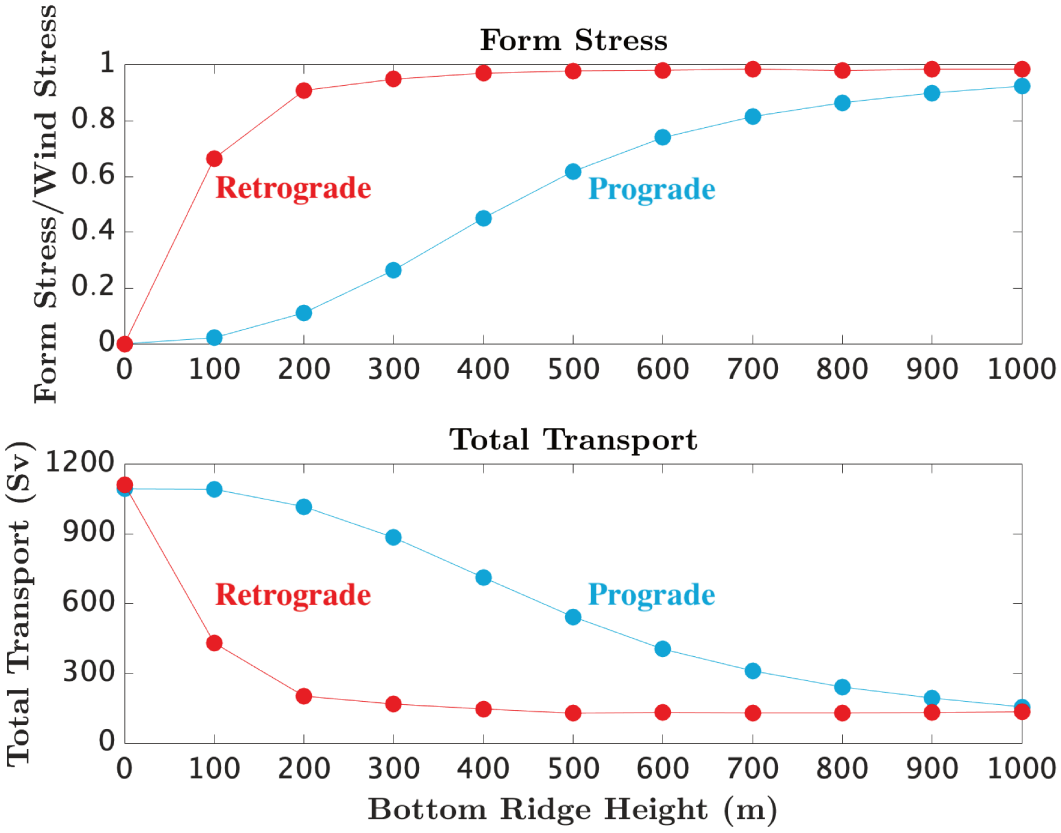

FIG. 4. Transition from friction-balanced to form topographic stress-balanced channel flows under retrograde (red) and prograde (blue) wind forcing. (Top) Fraction of the wind forcing that is balanced by topographic form stress. (Bottom) Total zonal transports.

significant in setting the topographic form stress ratio R_{TFS} or total transport T in prograde flows, such as surface wind forcing. We now test this hypothesis using a series of experiments in which we covary the bottom elevation cases ($H_{\mathrm{b}} = 100\,\mathrm{m}$, $H_{\mathrm{b}} = 300\,\mathrm{m}$, and $H_{\mathrm{b}} = 500\,\mathrm{m}$) with either the wind stress ($\tau_0 = \pm 0.05\,\mathrm{N\,m^{-2}}$ to $\pm 0.15\,\mathrm{N\,m^{-2}}$) or the quadratic drag coefficient ($C_{\mathrm{d}} = 1\times10^{-3}$ to 3×10^{-3}). The ranges of wind strengths and drag coefficients are inclusive of natural Southern Ocean wind variation and uncertainties in sea floor drag (Hogg et al. 2015; Lin et al. 2018; Liu et al. 2011). We then compare our results with previous studies of Southern Ocean circulation.

Fig. 5 shows the dependence of the topographic form stress ratio R_{TFS} and transports T and T_{BC} on the wind stress in both our prograde and retrograde experiments. The retrograde momentum balance is consistently dominated by topographic form stress, with the exception of the lowest ridge height $H_{\mathrm{b}} = 100\,\mathrm{m}$. These $H_{\mathrm{b}} = 100\,\mathrm{m}$ experiments have the largest baroclinic transport T_{BC}, due to a weakened meridional buoyancy flux and a weaker restratification by smaller-amplitude standing eddies (Abernathey and Cessi 2014; Wang and Stewart 2020), and the largest barotropic transport T_{BT}, as a more substantial contribution of the bottom friction and zonal bottom velocity is required in the momentum balance. Note that a non-monotonic relationship occurs between R_{TFS} and the surface wind stress at $H_{\mathrm{b}} = 100\,\mathrm{m}$. The definite reason for this is yet to be investigated, but in Section 4 we offer some potential insights using our "standing wave theory". Overall, retrograde zonal transports are relatively insensitive to the surface wind stress. Thus our retrograde experiments recover the "eddy saturated" regime that has been reported in various previous studies using eddy-resolving models of the ACC (Marshall et al. 2017; Munday et al. 2013; Hogg et al. 2008).

Our prograde experiments exhibit a markedly different sensitivity to wind stress from our retrograde experiments. Because bottom friction plays a non-negligible role in the momentum balance over this range of ridge heights (Fig. 4), one might anticipate that a stronger wind stress should be partially balanced by a stronger bottom friction, which requires a stronger zonal bottom flow. Fig. 5 confirms this expectation: R_{TFS} varies by less than ~15% over the range of wind stresses considered here, implying that a large fraction of the increases in wind-input momentum are balanced by changes in bottom friction, especially for H_b =

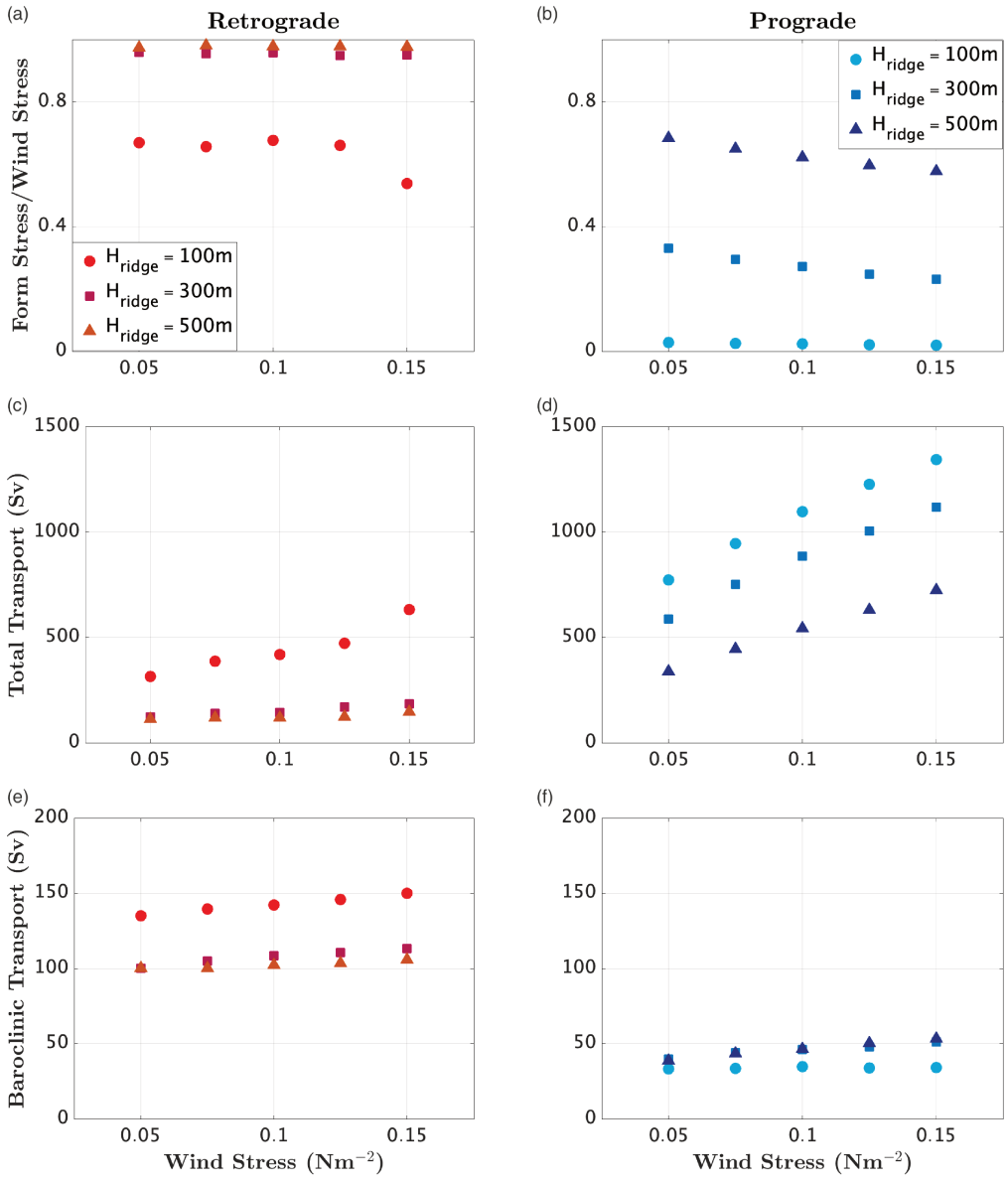

FIG. 5. Sensitivity of the zonal momentum balance zonal transport to the wind stress, τ_0, for various meridional ridge heights, H_b (see Table 1). (Top panels) Fraction of the wind forcing that is balanced by topographic form stress. (Middle panels) Depth-integrated zonal transport. (Bottom panels) Baroclinic component of the zonal transport (see Section 3).

100 m and 300 m. Consequently, T varies substantially with τ_0 for all three ridge heights, scaling generally as $T \propto (\tau_0 - C)^{1/2}$, in which C is some constant. In the limit of $H_b \to 0$, we expect a balance between surface wind stress and bottom friction, and therefore $T \propto \tau_0^{1/2}$. However, this strong sensitivity to prograde wind stress is confined to the barotropic transport; the baroclinic transport varies by only ~25% over the wind stress variations examined here, suggesting that prograde baroclinic flows are also approximately eddy-saturated.

Fig. 6 shows the dependence of R_{TFS} and T on the quadratic drag coefficient C_d. Note that, similarly, there exists a non-monotonic relationship between retrograde R_{TFS} and C_d at $H_\mathrm{b} = 100$ m. In Section 4, our "standing wave theory" yields some potential insight as to why this could occur. Overall, our retrograde experiments are relatively insensitive to the bottom drag coefficient, except in the special case of a very low ridge ($H_\mathrm{b} = 100$ m). Additionally, in $H_\mathrm{b} = 100$ m cases, albeit with a relatively insensitive barotropic transport, the bottom flow structure changes with C_d. At higher drag the zonal flow tends to

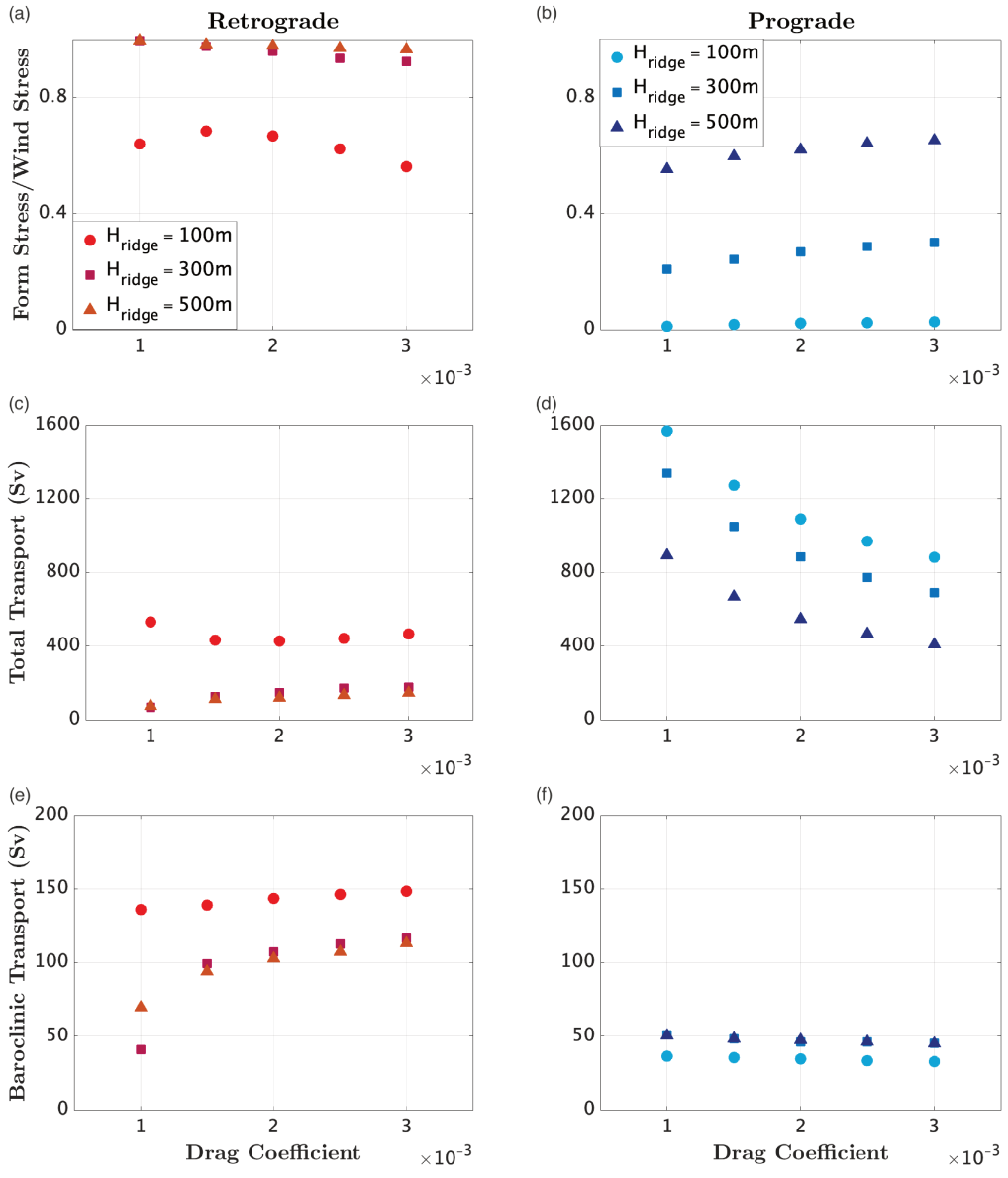

FIG. 6. Sensitivity of the zonal momentum balance zonal transport to the quadratic bottom drag coefficient, C_d, for various meridional ridge heights, H_b (see Table 1). (Top panels) Fraction of the wind forcing that is balanced by topographic form stress. (Middle panels) Depth-integrated zonal transport. (Bottom panels) Baroclinic component of the zonal transport (see Section 3).

spread out across the whole channel, while at lower drag a visibly strong jet develops (not shown). However, the baroclinic transport T_{BC} does vary by a factor of ~2 over the range of C_d explored here. Analogous results have been reported in the zonal circulation of ACC, and attributed to the frictional control of circumpolar currents (Marshall et al. 2017). In short, the suppression of nonlinear eddies by increased frictional drag allows stronger baroclinic flows to develop.

In our prograde experiments, the topographic form stress ratio R_{TFS} also exhibits a muted response to quadratic drag coefficient variations (Fig. 6). Larger quadratic drag coefficients allow for smaller bottom flow velocities, while still generating the required amount of bottom friction to close the momentum balance. R_{TFS} slightly increases as the drag coefficient increases, which requires even weaker bottom friction and thus further decreases the bottom flow speed required to close the momentum balance. This reduction in the bottom flow speed is reflected in the total prograde transport in Fig. 6. In contrast to the relative insensitivity of the retrograde transport to the drag coefficient, the prograde total transport drops by more than ~50% as the

bottom quadratic drag coefficient increases from 1×10^{-3} to 3×10^{-3}. However, similar to Fig. 5, the baroclinic transport T_{BC} does not vary with the drag coefficient, suggesting that, surprisingly, the baroclinic prograde flow is not susceptible to the frictional control described by Marshall et al. (2017). This could be because in prograde flows, the eddy field has a weaker feedback on the baroclinicity and stability of the mean flow. A more detailed investigation of these dynamics is left for future work.

4. Standing Wave Theory

In Section 3 we showed that there is a pronounced asymmetry in the momentum balances of retrograde and prograde channel flows. This qualitatively confirms our speculation in Section 1 that the inability of prograde flows to arrest Rossby wave propagation should suppress the development of topographic form stresses. In this section we attempt to quantitatively interpret our findings by posing a theory for the structure of the standing waves that emerge in our idealized channel. We then use this theory to predict the magnitude of the topographic form stress across our suite of sensitivity experiments. In Appendix A we perform an additional test of the theory against our continuously-stratified experiments using the MIT general circulation model (MITgcm, Marshall et al. 1997a,b).

We first derive closed-form solutions for the structure of a barotropic, quasi-geostrophic standing Rossby wave in our idealized channel. This idea was first posed by Davey (1980) in application to large-scale atmospheric problems. We derive our theory following Constantinou and Young (2017), who explored the effect of topography on beta-plane turbulence in oceanic environments. It is possible to extend the theory to a baroclinic system with multiple quasigeostrophic layers (see Abernathey and Cessi 2014). However, we restrict our attention to barotropic flows because this simplifies the dynamics and thus offers clearer insight into the mechanisms via which prograde and retrograde topographic form stresses are established.

Our starting point is the barotropic quasigeostrophic equations (*e.g.* Pedlosky 1987),

$$q_t + J(\psi, q) = -\frac{1}{\rho_0 H}\frac{\partial \tau}{\partial y} - \frac{r_b}{H}\zeta, \tag{13a}$$

$$q = \zeta + \beta y + \frac{f_0 \eta_b'}{H}, \tag{13b}$$

$$\zeta = \nabla^2 \psi. \tag{13c}$$

Here all symbols have identical notations as introduced in Section 2, except q has been rescaled by a factor of H, $\zeta = \hat{\boldsymbol{z}}\cdot\nabla\times\boldsymbol{u}$ denotes the relative vorticity, and $\eta_b' = \eta_b + H$ is the elevation of the ridge above the sea floor. For analytical simplicity we have replaced the quadratic drag used in (2) by a linear drag with drag velocity r_b.

To solve (13a)–(13c) we first split the flow $\boldsymbol{u}$ into a zonal-mean component, $U\hat{\boldsymbol{x}}$, and a perturbation component that describes the standing wave, $\boldsymbol{u}' = -\nabla\times\psi'\hat{\boldsymbol{z}}$,

$$\psi = -Uy + \psi'(x, y). \tag{14}$$

We then seek a steady solution ($\partial/\partial t \equiv 0$) and assume that meridional variations of the flow bathymetry and the wind stress are vanishingly small. Under these assumptions, (13a) simplifies approximately to

$$\underbrace{U\frac{\partial^3\psi'}{\partial x^3}}_{\text{Relative vorticity advection}} + \underbrace{U\frac{f_0}{H}\frac{\partial \eta_b'}{\partial x}}_{\text{Topographic vorticity generation}} + \underbrace{\beta\frac{\partial\psi'}{\partial x}}_{\text{Planetary vorticity advection}} = \underbrace{-\frac{r_b}{H}\frac{\partial^2\psi'}{\partial x^2}}_{\text{Frictional vorticity damping}}. \tag{15}$$

We then exploit the linearity of (15) to derive a solution in terms of Fourier series, *e.g.*

$$\psi' = \Re\left\{\sum_k \hat{\psi}_k\, e^{ikx}\right\}, \tag{16}$$

where k is the wavenumber and $\Re$ denotes the real part. We apply (16) to both ψ' and η_b, substitute the result into (15), and then rearrange to obtain

$$\hat{\psi}_k = \frac{f_0}{k^2}\frac{U\left(U + c_k + i\frac{r_b}{Hk}\right)}{(U+c_k)^2 + \left(\frac{r_b}{kH}\right)^2}\frac{(\hat{\eta}_b)_k}{H}. \tag{17}$$

Here $c_k = -\beta/k^2$ is the barotropic Rossby wave phase speed. Eqn. (17) states that the Fourier modes of the standing wave streamfunction are proportional to the corresponding modes of the bathymetry. The coefficient of proportionality in (17) has both real and imaginary parts, yielding components of the streamfunction that are in phase and out of phase with the bathymetry variations, respectively. The imaginary, out-of-phase component is proportional to r_b, indicating that bottom friction serves to shift the streamfunction such that it is out of phase with the bathymetry.

To complete the solution we must additionally solve for the unknown mean flow speed U. We use the zonally-averaged momentum equation corresponding to (13a), which may be written as

$$0 = \underbrace{\frac{\tau}{\rho_0}}_{\text{Wind Stress}} \underbrace{- r_b U}_{\text{Friction}} \underbrace{+ f_0\overline{\psi_x'\eta_b'}^{\,x}}_{\text{Form Stress}}. \tag{18}$$

We evaluate the form stress term using our solution (17) for ψ', which yields

$$f_0\overline{\psi_x'\eta_b'}^{\,x} = -\frac{1}{2}\sum_k \frac{|(\hat{\eta}_b)_k|^2}{H^2}\cdot\frac{r_b U f_0^2/k^2}{(U+c_k)^2 + \left(\frac{r_b}{kH}\right)^2} \tag{19}$$

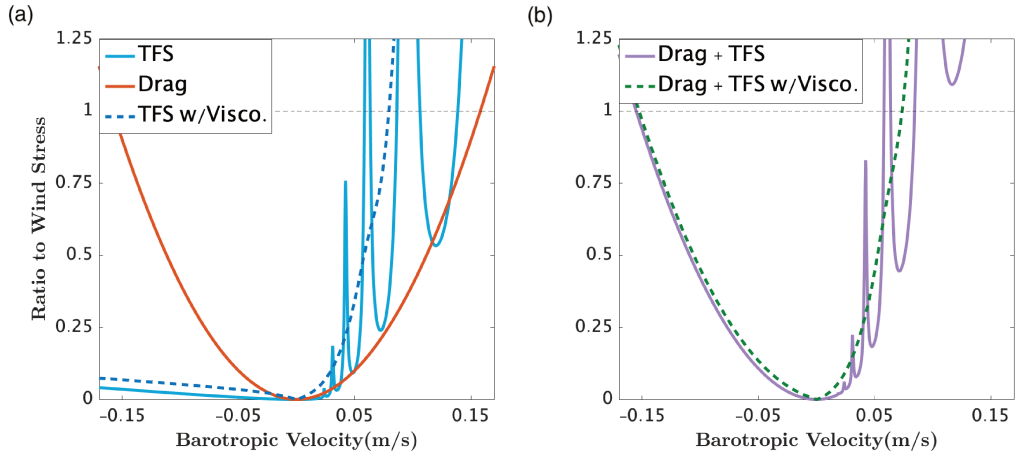

FIG. 7. (Left) Illustration of the dependence of the theoretically-predicted topographic form stress (TFS) and bottom friction (Drag) on the barotropic mean flow velocity (U). The TFS is shown with and without the addition of an eddy viscosity of $\nu = 1000\,\mathrm{m^2\,s^{-1}}$ (see Section 4 and Appendix B). We use a ridge height of 150 m, and other parameters match those given in Table 1. All terms are normalized by the wind stress, so the horizontal dashed line corresponds to the zonal force that balances the wind stress. (Right) As in the left panel, but showing the sum of the TFS and bottom friction terms, again with and without eddy viscosity. The crossing of the sum with 1 corresponds to U values that balance the theoretical momentum budget (18).

Note that the form stress results entirely from the component of $\hat{\psi}$ that is out of phase with the bathymetry, which in (17) is proportional to the linear drag coefficient r_b. Thus bottom friction plays a key role in establishing the form stress by shifting the streamfunction out of phase with the bathymetric variations. Note also that the sign of the topographic form stress (19) is always opposite to that of the mean flow, consistent with its role in retarding the mean flow in both our prograde and retrograde experiments in Section 3.

Finally, we solve for U, and thus ψ', by substituting Eqn. (19) into (18). For monochromatic bathymetry (*i.e.* a single wavenumber k) this would yield a quadratic equation for U that could be solved analytically. However, in general a spectrum of wavenumbers contribute to the bathymetry and the form stress, so we solve (18)–(19) numerically. We additionally make the further approximation $r_b = C_\mathrm{d}|U|$, which is valid in the limit of weak standing wave flow (relative to the strength of the mean flow, U), though the results do not differ qualitatively from those obtained by selecting a constant r_b. In all of the solutions discussed below we account for the meridionally varying surface wind profile by solving (18)–(19) separately at each latitude y, allowing us to construct a two-dimensional standing wave streamfunction via (14).

In Fig. 7(a) we illustrate the behavior of the solution by plotting the friction and form stress terms in the quasi-geostrophic momentum equation (18) as functions of the mean flow U. All parameters take their reference values from Table 1, except we use a relatively low ridge height ($H_\mathrm{b} = 150\,\mathrm{m}$) to better visualize the structures of the curves and to make the differences between retrograde and prograde cases easier to discern. While the bottom friction term has a simple quadratic dependence on U (due to our assumption that $r_b = C_\mathrm{d}|U|$), the topographic form stress exhibits a pronounced asymmetry between prograde and retrograde flows. In particular, the topographic form stress increases much more sharply as the retrograde flow ($U > 0$) strengthens than it does as the prograde flow ($U < 0$) strengthens. The topographic form stress also exhibits sharp variations and "spikes" as a function of U for $U > 0$; these occur when the flow speed exactly matches the barotropic Rossby wave phase speed at different wavenumbers, *i.e.* $U + c_k = 0$ for some k. This causes the denominator of (19) to become very small in magnitude, and thus greatly increases the contribution of the corresponding streamfunction component $\hat{\psi}_k$ to the topographic form stress.

A consequence of the non-monotonic dependence of the topographic form stress on U is that there may be multiple solutions (see Constantinou and Young 2017), *i.e.* multiple zonal mean flow strengths U that satisfy the momentum balance (18). An example of such a case is shown in Fig. 7(b): the sum of the bottom friction and topographic form stress matches the wind stress (indicated by the crossings of the "sum" curve with 1) at three different mean flow speeds for $U > 0$, *i.e.* for retrograde flow. This may explain the non-monotonic dependence of R_TFS on surface wind stress (Fig. 5) and bottom drag (Fig. 6) in some of our retrograde experiments. A slight change in the barotropic velocity can shift the R_TFS to a larger or smaller value depending on the initial position on the "sum" curve. For the purposes of comparing the theoretically-predicted topographic form stress ratio R_TFS with that diagnosed from

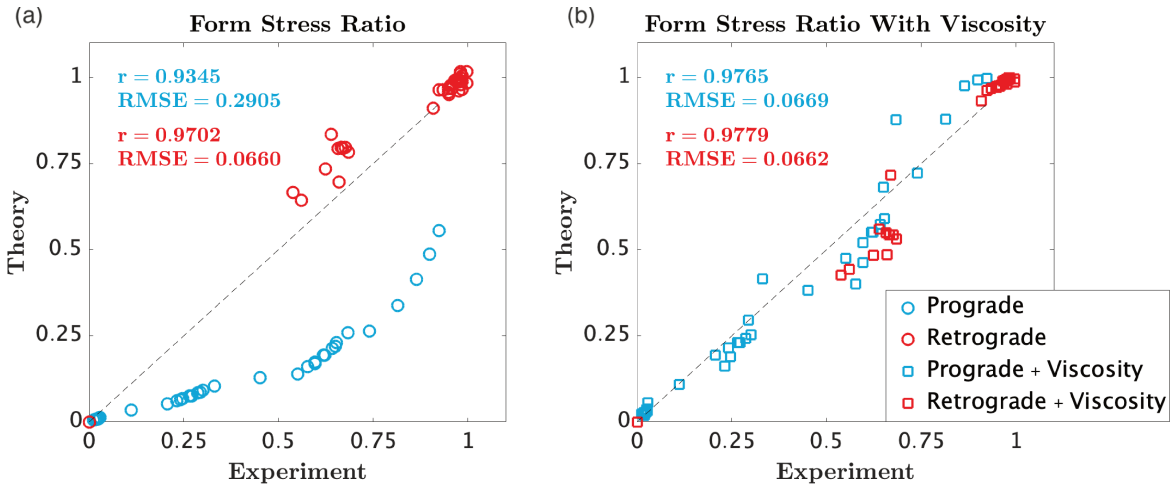

FIG. 8. Evaluation of our standing wave theory against our isopycnal model experiments in a flat-bottomed channel with a meridonal ridge (see Sections 2–4). The experimentally diagnosed and theoretically predicted topographic form stress ratios R_{TFS} are scattered against one another for each of our sensitivity experiments (Section 3). The panels show the result without (a) and with (b) an eddy viscosity of $\nu = 1000\,\mathrm{m^2\,s^{-1}}$ in the standing wave theory (see Appendix B). Pearson correlation coefficients (r) and root-mean-square errors (RMSE) are given separately for the prograde and retrograde cases in each panel, quantifying the deviation of the data correlation from a purely linear relationship and the differences between theory predictions and experimental results, respectively. The significance level for all correlation analyses is 0.01.

our simulations, we simply take the average of the topographic form stress across all viable solutions. However, the multiplicity of solutions also introduces discontinuity in the solution constructed via (14), as solution branches appear and disappear with varying latitude y. We therefore additionally present results obtained by applying a simple regularization to the standing wave solution, imposing an eddy viscosity of $1000\,\mathrm{m^2/s}$ in (13a). This solution is discussed further in Appendix B.

In Fig. 2(c–d) we illustrate the two-dimensional structure of the solution of the standing wave theory, using parameters that match our reference prograde and retrograde simulations (Fig. 2(a–b)). We use an eddy viscosity in both cases to eliminate discontinuities in the retrograde solution. The standing wave solutions visibly capture the structure of the barotropic transport in both our prograde and retrograde solutions, and matches the zonal transport in both cases to within 5 % (retrograde 3.73 %; prograde 4.93 %). Differences are most pronounced in regions with relatively rapid meridional variations in the streamfunction, which violate the assumptions of the theory. This comparison suggests that the standing wave theory qualitatively captures the structure and transport of the simulated flow, despite various simplifying assumptions and the neglect of baroclinicity, and thus is an appropriate tool for interpreting prograde/retrograde asymmetries in the establishment of topographic form stress.

To further evaluate the predictions of our standing wave theory, in Fig. 8 we compare the topographic form stress ratio R_{TFS} predicted by the theory against those diagnosed from the suite of sensitivity experiments described in Section 3. For completeness, we perform this comparison with and without the inclusion of eddy viscosity in the theory. For both prograde and retrograde flows, the theory approximately captures the transition from a frictionally-dominated momentum balance ($R_{\mathrm{TFS}} = 0$) to a form stress-dominated momentum balance ($R_{\mathrm{TFS}} = 1$), which is primarily controlled by the height of the ridge (see Section 3). However, the theory tends to somewhat underpredict the strength of the topographic form stress in prograde flows unless the eddy viscosity is included. This is likely because the eddy viscosity enhances the phase shift between the streamfunction and the bathymetry, and thus favors stronger topographic form stresses (see Appendix B). By contrast, despite the necessity of the eddy viscosity to regularize the standing wave solution in the retrograde case, it has relatively little impact on the predicted R_{TFS}.

The close agreement between the predictions of the standing wave theory and the diagnostics from our simulations allows us to use the theory to interpret the asymmetry between prograde and retrograde momentum balances. We pose the following exposition in spectral space, rather than in real space, to clarify the interpretation. Our theory reveals that the mechanism of topographic form stress generation is fundamentally the same in both prograde and retrograde flows: the bottom friction produces a phase lag between the bathymetry and the standing wave streamfunction, and thus between the bathymetry and the pressure field (Eqn. 17). In prograde flows this effect is typically weak because the frictional vorticity damping term in (15) is much weaker than the conservative terms on the left-hand side, *i.e.* typically $r_b k/\beta H \ll 1$. Thus

the topographic vorticity generation by the mean flow U is primarily balanced by relative vorticity advection and planetary vorticity advection. A small contribution from bottom frictional damping is required by the flow vorticity balance, meaning that a less visible phase lag is induced as shown in Fig. 2(b,d). By contrast, in retrograde flows, only planetary vorticity advection opposes the topographic vorticity generation in (15), *i.e.* relative vorticity advection compensates and enhances the topographic vorticity generation. A greater frictional damping is therefore expected to close the vorticity balance, which translates to a more severe phase lag (see Fig. 2(a,c)). In short, the degree to which the topographic vorticity generation is balanced by frictional damping determines the amplitude of the TFS, for a given flow speed U. The most extreme example of this occurs for monochromatic topography with wavenumber $k = k_0$: when the mean flow speed exactly opposes the Rossby wave speed, $U + c_k = 0$, the sum of the relative vorticity advection and planetary vorticity advection terms vanishes. In this situation the topographic vorticity generation must be balanced entirely by friction, yielding a standing wave that is perfectly 90° out of phase with the bathymetry, maximizing the topographic form stress.

5. Experiments with Continental Shelf/Slope Bathymetry

Thus far, we have only investigated the establishment of topographic form stress, and its influence on setting the zonal transport, in a flat-bottomed channel with a single meridional ridge (hereafter "a flat-bottomed channel"). This idealization is commonly used to model the ACC (*e.g.* Hallberg and Gnanadesikan 2001; Stewart and Thompson 2013; Abernathey and Cessi 2014; Howard et al. 2015; Patmore et al. 2019), which is a retrograde current system. However, in nature prograde current systems often occur over continental slopes, as discussed in Section 1. Anticipating that the presence of a continental shelf and slope bathymetry should modify the standing wave interaction with the mean flow, we now conduct an additional suite of experiments using a continental shelf/slope-like bathymetry. Then, extending our standing wave theory to the continental shelf/slope geometry, we evaluate the transferability of our findings and interpretation in terms of standing waves to prograde currents in nature.

Fig. 9 illustrates the continental slope/shelf-like model configuration deployed in our study. We use a continental slope much broader, and a continental shelf much shallower, than those found in nature, in order to avoid isopycnal layers incropping/outcropping at the sea floor or ocean surface, which would substantially complicate the dynamics. Specifically, we prescribe the bathymetry as

$$\eta_b(x,y) = -h_s(y - Y_s(x)) \tag{20a}$$

$$h_s(\tilde{y}) = H - \tfrac{1}{2}H_s\left[1 - \tanh\left(\frac{\tilde{y}}{W_s}\right)\right], \tag{20b}$$

$$Y_s(x) = Y_s^0 + \Delta Y_s \operatorname{sech}\left(\frac{x - L_x/2}{L_s}\right)^2, \tag{20c}$$

where $H_s = 2000\,\mathrm{m}$ is the height of the shelf, $W_s = 250\,\mathrm{km}$ is the half-width of the slope, and $Y_s^0 = 800\,\mathrm{km}$ is the latitude of the slope center in our reference experiment. Rather than impose a uniform meridional ridge, as in Section 2, we impose a meridional excursion of the continental slope with amplitude $\Delta Y_s = 700\,\mathrm{km}$ and zonal half-length $L_s = 100\,\mathrm{km}$. We also center the surface wind stress over the continental slope, prescribing

$$\tau(y) = \begin{cases} \tau_0 \cos^2\left(\dfrac{\pi(y - Y_s^0)}{2Y_s^0}\right), & y \le 2Y_s^0, \\ 0, & y \ge 2Y_s^0. \end{cases} \tag{21}$$

In Fig. 10 we contrast the momentum balances in prograde and retrograde flows over continental shelf/slope-like bathymetry. The results are qualitatively similar to those from our flat-bottomed channel simulations, shown in Fig. 3. Retrograde momentum imparted by the surface wind stress is almost completely balanced by topographic form stresses established across the protrusion of the continental slope. In this case there are also relatively weak, alternating contributions from advection and bottom friction, associated with the formation of multiple jets across the continental slope (see Fig. 9 and Vallis and Maltrud (1993)). In the prograde case, the wind-input momentum is balanced by both topographic form stress, primarily toward the base of the continental slope, and by bottom friction, primarily toward the top of the continental slope. This suggests that our conclusions regarding the asymmetry in the establishment of topographic form stresses in prograde and retrograde flows are not fundamentally altered by the more complex shelf/slope-like geometry.

Motivated by the qualitative similarity of the continental shelf/slope and flat-bottomed channel momentum budgets, we now test the potential for our standing wave theory to explain the prograde/retrograde asymmetry over continental shelf/slope-like bathymetry. The theory follows Section 4, but must be modified to account for meridional bathymetric variations. We therefore assume that the bathymetry along each latitude band $y = y_0$ can be locally approximated as a linear meridional slope, given by the meridionally-uniform component of the bathymetry (20a)–(20c), plus a zonal

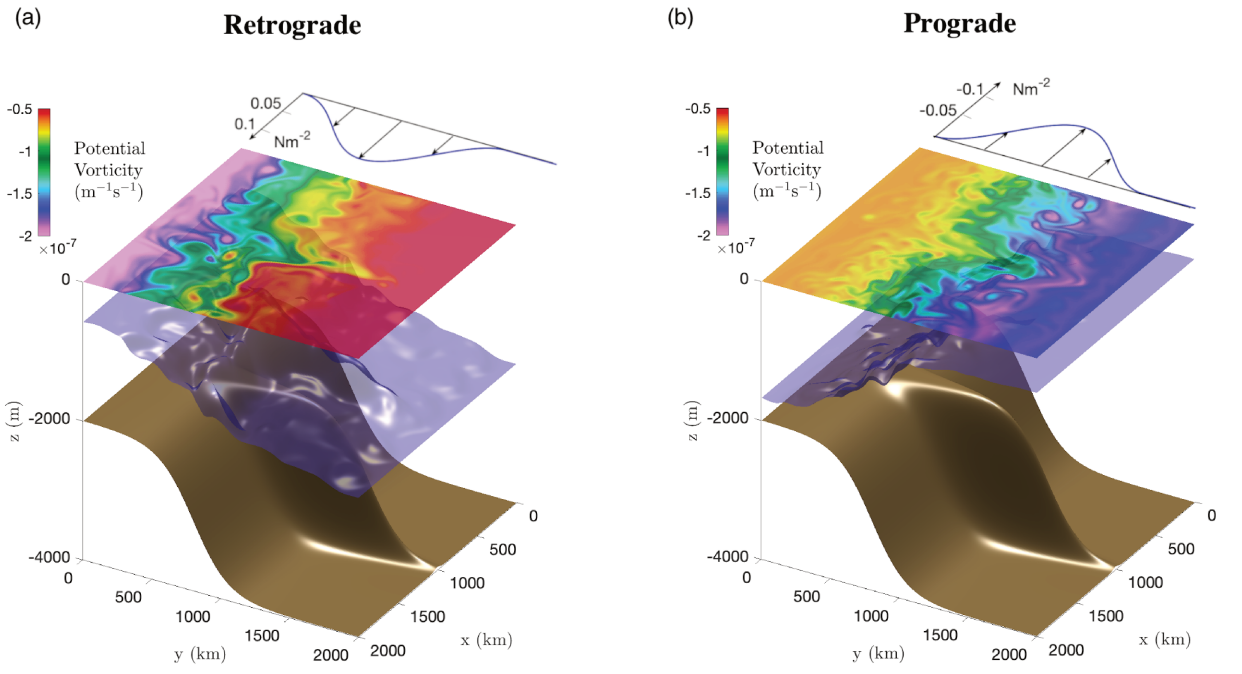

FIG. 9. As Fig. 1, but for our simulations in a continental shelf/slope-like geometry. Note that $y = 0$ km corresponds to the southern boundary of our model domain.

perturbation:

$$\eta_b(x, y_0) \approx -h_{\mathrm{QG}}(y_0) + s_{\mathrm{QG}}(y_0) \cdot (y - y_0) + \eta_b'(x), \quad (22)$$

$$h_{\mathrm{QG}}(y) = h_s\left(y - Y_s^0\right), \quad (23)$$

$$s_{\mathrm{QG}}(y) = -\frac{\partial}{\partial y}\left[h_{\mathrm{QG}}\left(y - Y_s^0\right)\right]. \quad (24)$$

Under this assumption, the quasigeostrophic potential vorticity equations (13a)–(13b) can be approximated in the vicinity of $y = y_0$ as

$$q_t + J(\psi, q) = -\frac{1}{\rho_0 h_{\mathrm{QG}}}\frac{\partial \tau}{\partial y} - \frac{r_b}{h_{\mathrm{QG}}}\zeta, \quad (25a)$$

$$q = \zeta + (\beta + \beta_t)y + \frac{f_0 \eta_b'}{h_{\mathrm{QG}}}, \quad (25b)$$

where $\beta_t = f_0 s_{\mathrm{QG}}(y_0)/h_{\mathrm{QG}}(y_0)$ is the 'topographic β' (Vallis and Maltrud 1993). The standing wave theory then follows as derived in Section 4, but with H replaced by $h_{\mathrm{QG}}(y)$ and β replaced by $\beta + \beta_t$ throughout.

Fig. 11 serves both to evaluate the relevance of standing wave theory to flows over a continental shelf/slope-like geometry, and to quantify the dependence of the topographic form stress ratio R_{TFS} on the geometry of the protrusion from the continental slope. Specifically, we perform a series of experiments in which we vary the amplitude ΔY_s and length L_s of the protrusion, and compare the resulting momentum balance in each experiment against the corresponding prediction of the standing wave theory. In contrast to the flat-bottomed channel (Fig. 8), with continental shelf/slope-like geometry the theory consistently underpredicts R_{TFS} under retrograde wind forcing, although the theoretical prediction and experimental diagnostics remain closely correlated. This underprediction may occur because the theory cannot reproduce the meridional redistribution of momentum by advective fluxes (see Fig. 10), which in some cases leads to a reversal of the domain-integrated bottom friction and thus $R_{\mathrm{TFS}} > 1$. By contrast, the prograde momentum balance remains predicted by the standing wave theory, regardless of whether an eddy viscosity is included in the theory. Fig. 11 also shows that the retrograde momentum balance is most primarily controlled by the zonal length of the continental slope excursion, L_s, which determines the zonal gradient of topography, thus the topographic form stress. By contrast, the prograde momentum balance depends on both L_s and the amplitude of the continental slope excursion, ΔY_s. Furthermore, the prograde topographic form stress never balances more than 50% of the wind stress over the range of shelf/slope geometric parameters explored in this study.

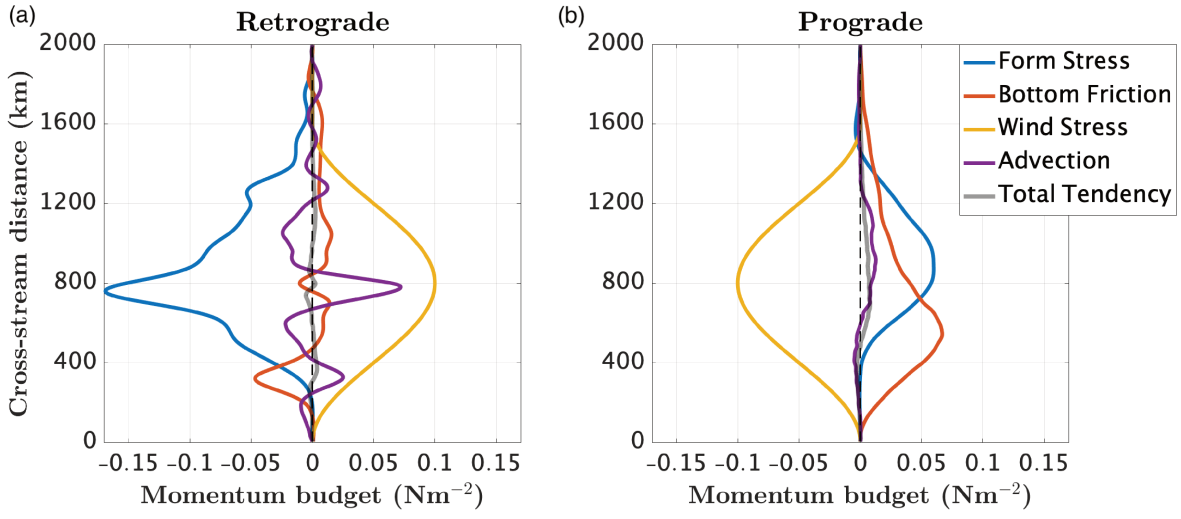

FIG. 10. As Fig. 3, but diagnostics drawn from our continental shelf/slope simulations.

6. Discussion and conclusion

In this study we have used a high-resolution isopycnal channel model (Fig. 1) to investigate the role of topographic form stress in balancing prograde wind-driven flows, *i.e.* flows opposing the direction of Rossby wave propagation. Topographic form stress has been repeatedly demonstrated to balance wind-input retrograde momentum in the Antarctic Circumpolar Current (Munk and Palmén 1951; Stevens and Ivchenko 1997; Ward and Hogg 2011; Masich et al. 2015). However, the momentum balance, and thus the sensitivity to wind stress, of prograde current systems is relatively poorly understood. In Section 1 we speculated that the inability of prograde flows to arrest Rossby wave propagation should suppress the influence of topographic form stress (Thompson and Naveira Garabato 2014; Marshall 2016), and thus potentially render prograde currents more sensitive to changes in near-surface winds.

In Section 3 we showed that prograde and retrograde flows may establish qualitatively different momentum balances, despite otherwise identical geometries and forcings. Specifically, while topographic form stress primarily balances the retrograde wind stress, the prograde wind stress is primarily balanced by bottom friction (Fig. 3). In this regime, the dependence of the prograde momentum balance on bottom friction leads to a relatively strong sensitivity of the zonal transport on the surface wind stress (Fig. 5) and bottom drag coefficient (Fig. 6). However, topographic form stress can almost entirely balance a prograde wind stress, provided that variations in the sea floor elevation are sufficiently large (Fig. 4). These findings suggested that the alignment of the mean flow and Rossby wave propagation does indeed suppress topographic form stress, but only partially so.

To interpret our experimental findings, in Section 4 we posed a quasigeostrophic, barotropic theory for wind-forced standing Rossby waves. Our theory captured the dominant structure of the simulated depth-integrated streamfunction and predicted the zonal transport within 5 %. The theory also qualitatively and quantitatively reproduced the relative importance of topographic form stress in the momentum balance across our suite of perturbation experiments (Fig. 8). This agreement motivated an interpretation of our central findings in terms of barotropic standing Rossby waves: in both the prograde and retrograde cases, the topographic form stress arises because non-conservative effects (bottom friction and eddy potential vorticity fluxes) shift the zonal phase of the bottom pressure field away from that of the bathymetry. However, this mechanism is substantially more efficient in retrograde flows. This asymmetry is most easily understood in the extreme case of bathymetry of a single wavelength: when the flow speed arrests barotropic Rossby waves of exactly that wavelength, the standing wave is exactly out of phase with the bathymetry (Eqn. (15)) and thus the topographic form stress is maximized (Eqn. (19)).

As noted in Section 1, in nature prograde current systems often arise over continental slopes, such as the Antarctic Slope Current (Thompson et al. 2018) and the East and West Greenland Currents (Brearley et al. 2012; Myers et al. 2009). In Section 5 we therefore adapted our experimental configuration and theory to a geometry that qualitatively resembles a continental shelf and slope (Fig. 9). Consistent with the flat-bottomed channel experiments (Fig. 10), we found that over the continental shelf/slope geometry the asymmetry of topographic form stress generation between prograde and retrograde experiments still holds. Additionally, the standing wave theory continued to closely pre-

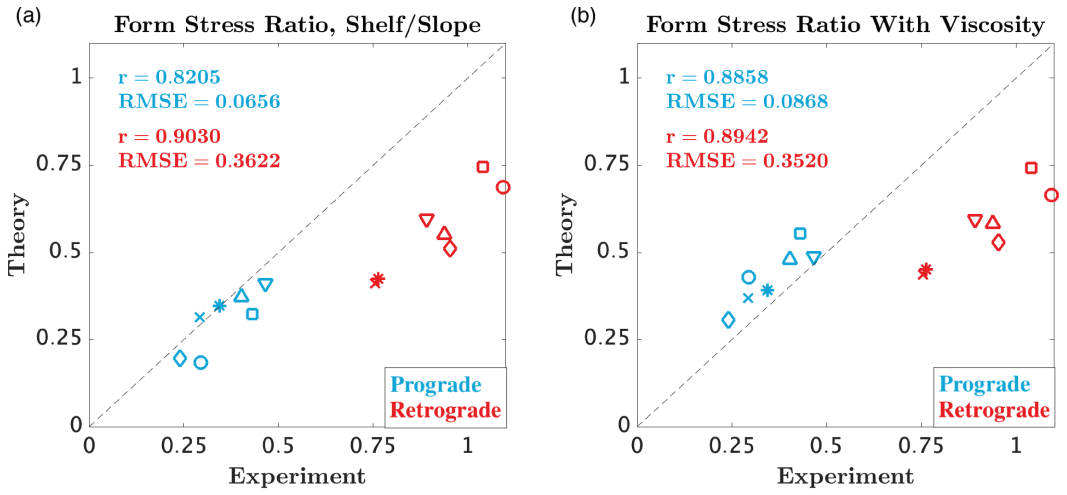

FIG. 11. As Fig. 8, but diagnostics drawn from our continental shelf/slope simulations. The marker shapes indicate our sensitivity experiments as follows. ○: $L_s = 100\,\text{km}$, $\Delta Y_s = 500\,\text{km}$; □: $L_s = 100\,\text{km}$, $\Delta Y_s = 700\,\text{km}$; ◇: $L_s = 200\,\text{km}$, $\Delta Y_s = 500\,\text{km}$; △: $L_s = 200\,\text{km}$, $\Delta Y_s = 800\,\text{km}$; ▽: $L_s = 200\,\text{km}$, $\Delta Y_s = 1000\,\text{km}$; ×: $L_s = 400\,\text{km}$, $\Delta Y_s = 800\,\text{km}$; and ∗: $L_s = 400\,\text{km}$, $\Delta Y_s = 1000\,\text{km}$.

dict the partitioning of the prograde momentum balance over continental shelf/slope bathymetry, suggesting that this theory might provide dynamical insight into prograde slope current systems in the ocean.

Our minimal, two-layer isopycnal model of wind-driven baroclinic circulation in a channel has allowed us to isolate the differences between prograde and retrograde momentum balances. However, this idealization differs from ocean current systems non-negligibly in various respects, and there are many possible extensions of the present work that would allow for closer comparisons with prograde current systems in nature. For example, prograde current systems in nature typically do not form continuous loops that are directly comparable to the Antarctic Circumpolar Current; even though Antarctica and Greenland are surrounded by closed isobaths, the prograde current systems there do not fully encircle their respective land masses. Over a finite along-current distance, the momentum balance includes additional contributions due to along-current pressure gradients that are not considered here. A related challenge is that the coordinate system in which to pose the momentum balance is less obvious over a winding continental slope; for example, selecting a coordinate system that follows isobaths eliminates the topographic form stress entirely (Stewart et al. 2019). In the Antarctic Circumpolar Current there is a well-established focus on the zonal momentum balance, yet even there one obtains different perspectives on the dynamics in zonal vs. along-streamline coordinates (Abernathey and Cessi 2014).

The simplified physics of our isopycnal model also excludes various additional contributors to the circulation of retrograde and prograde current systems. For example, wind forcing only partially explains the structure and transport of the Antarctic Circumpolar Current: buoyancy forcing also plays a significant role in setting the mean transport (*e.g.* Hogg 2010; Howard et al. 2015). Buoyancy forcing also contributes substantially to the structure of prograde current systems over continental slopes (*e.g.* Hattermann 2018; Spall 2004), as does the rectification of tidal motions (Robertson et al. 1998; Stewart et al. 2019). While buoyancy forcing does not directly influence the momentum budget, the presence of sea ice may substantially influence the transfer of momentum from the atmosphere to the ocean and ultimately to the solid Earth (Meneghello et al. 2018; Stewart et al. 2019). Our model also incompletely represents the mechanisms of momentum and energy extraction at the sea floor: the Antarctic Circumpolar Current has been shown to be substantially influenced via the drag associated with generation of internal lee waves (Yang et al. 2018; Naveira Garabato et al. 2013). The influence of this mechanism on prograde current systems remains to be established.

As prograde current systems tend to be situated on continental slopes, their momentum balance is relevant to cross-slope exchange; vertical convergence and divergence of momentum fluxes are directly related to cross-slope isopycnal transport (Stewart and Thompson 2015b; Stewart 2019). Here we have focused on the depth-integrated momentum balance, but the prograde/retrograde asymmetry might also introduce dynamically relevant differences in the baroclinic stability and dynamics of the eddy field, and the partitioning of the interfacial form stress between transient and standing components. Extending the current work to obtain an idealized process-level understanding of these phenomena in prograde flows may also be valuable. However, as noted by Abernathey and Cessi (2014), a complete picture of the interaction between the mean flow and the eddies remains out of reach because the relationship

between the mean flow structure and the eddy diffusivity remains elusive, particularly over continental slopes (Wang and Stewart 2020). A further complication is that the relevance of quasigeostrophic theory becomes questionable when the sea floor elevation changes are comparable to the mean ocean depth, and when isopycnals incrop/outcrop at the sea floor and surface (Pedlosky 1987). Another related source of asymmetry, not explored here, is the tendency for mesoscale variability to produce rectified prograde flows over steep continental slopes (Holloway et al. 1989), even when the mean flow is dominantly retrograde (Wang and Stewart 2018; Manucharyan and Isachsen 2019). The findings of this study should therefore be regarded as a step toward a more complete conceptual understanding of the mean and transient dynamics of prograde current systems.

Acknowledgments. This material is based in part upon work supported by the National Science Foundation under Grant Numbers OPP-1543388 and OCE-1751386. YW is supported by the Research Grants Council of Hong Kong (ECS26307720), and the Center for Ocean Research (CORE), a joint research center between QNLM and HKUST. This work used the Extreme Science and Engineering Discovery Environment (XSEDE, Towns et al. 2014), which is supported by National Science Foundation grant number ACI-1548562. The authors thank Geoff Stanley and another anonymous reviewer for many constructive comments that improved the submitted manuscript.

Data availability statement. The AWSIM model code used in this study can be obtained from `https://github.com/andystew7583/AWSIM`.

APPENDIX A

MITgcm configuration

A shortcoming of our two-layer isopycnal model (Section 2) is its low vertical resolution. This limits the model to representing a single baroclinic mode, and limits the classes of unstable baroclinic waves that can grow and form transient eddies (*e.g.* Vallis 2006). We therefore reproduce a key subset of our two-layer sensivity experiments in a flat-bottomed channel (see Section 3) using the MIT general circulation model (MITgcm, Marshall et al. 1997a,b). The model configuration approximately matches that described in Section 2: below we describe salient differences between the model configurations. Fig. A12 shows the model domain with a typical flow configuration, the surface wind forcing, and the zonal-/time-mean stratification and zonal flow. A list of relevant model parameter values is given in Table A2.

We use the MITgcm to evolve the model state via the hydrostatic Boussinesq primitive equations. Potential temperature is the only thermodynamic variable, and we use a linear equation of state with a thermal expansion coefficient of $\alpha = 1\times10^{-4}\,\mathrm{K}^{-1}$. To avoid a drift in the simulated stratification, we restore the potential temperature at the northern boundary, with a restoring rate that varies linearly from $7\,\mathrm{days}^{-1}$ at $y = L_y$ to zero at $y = L_y - L_r$, where $L_r = 100\,\mathrm{km}$. Grid-scale accumulation of energy and enstrophy is controlled via horizontal and vertical viscous operators, listed in Table A2. We parameterize wind-driven vertical mixing close to the surface and shear-driven mixing in the interior using the K-profile parameterization (Large et al. 1994), and impose a uniform background vertical diffusivity of $\kappa_v = 5\times10^{-6}\,\mathrm{m^2\,s^{-1}}$. The model equations are discretized on a uniform horizontal grid with spacing 12.5 km, on a 70-level vertical grid whose spacings range from 10.5 m at the surface to 103.8 m at the sea floor. We ran several simulations with a finer, 6.5 km horizontal grid to verify that the resolution of the eddy field was not influencing our results.

In Figs. A13 and A14 we reproduce Figs. 4 and 8 using a sequence of MITgcm experiments with varying ridge heights H_b. In both figures the diagnostics from the MITgcm experiments qualitatively resemble those from our isopycnal model experiments, though there are some quantitative differences due to differences in the model parameters (particularly the planetary β). In particular, the MITgcm experiments recover the pronounced asymmetry

TABLE A2. List of parameters used in our MIT general circulation (MITgcm, Marshall et al. 1997a,b) reference simulation.

	Value	Description
L_x	2000 km	Zonal domain size
L_y	2000 km	Meridional domain size
H	4000 m	Maximum ocean depth
Y_w	1000 km	Peak wind stress position
H_b	400 m	Bottom ridge height
X_b	−500 km	Bottom ridge zonal position
W_b	400 km	Bottom ridge width
ρ_0	1000 kg m^{-3}	Reference density
α	$1\times10^{-4}\,\mathrm{K}^{-1}$	Thermal expansion coefficient
g	9.81 m^2 s^{-1}	Gravitational constant
f_0	$-1.32\times10^{-4}\,\mathrm{s}^{-1}$	Coriolis parameter
β	$9.63\times10^{-12}\,\mathrm{s}^{-1}\mathrm{m}^{-1}$	Coriolis parameter gradient
T_r	7 days	Northern relaxation timescale
L_r	100 km	Width of northern relaxation region
τ_0	0.1 N m^{-2}	Wind stress maximum
C_d	2×10^{-3}	Quadratic drag coefficient
$A_{4,\mathrm{grid}}$	0.1	Grid-dependent horizontal biharmonic viscosity
A_h	$12\,\mathrm{m^2s^{-1}}$	Laplacian horizontal viscosity
A_v	$3\times10^{-4}\,\mathrm{m^2s^{-1}}$	Laplacian vertical viscosity
κ_v	$5\times10^{-6}\,\mathrm{m^2s^{-1}}$	Laplacian vertical diffusivity
Δ_h	12.5 km, 6.25 km	Horizontal grid spacing
Δ_z	10.5 m–103.8 m	Vertical grid spacing
Δt	897 s, 448 s	Time step size

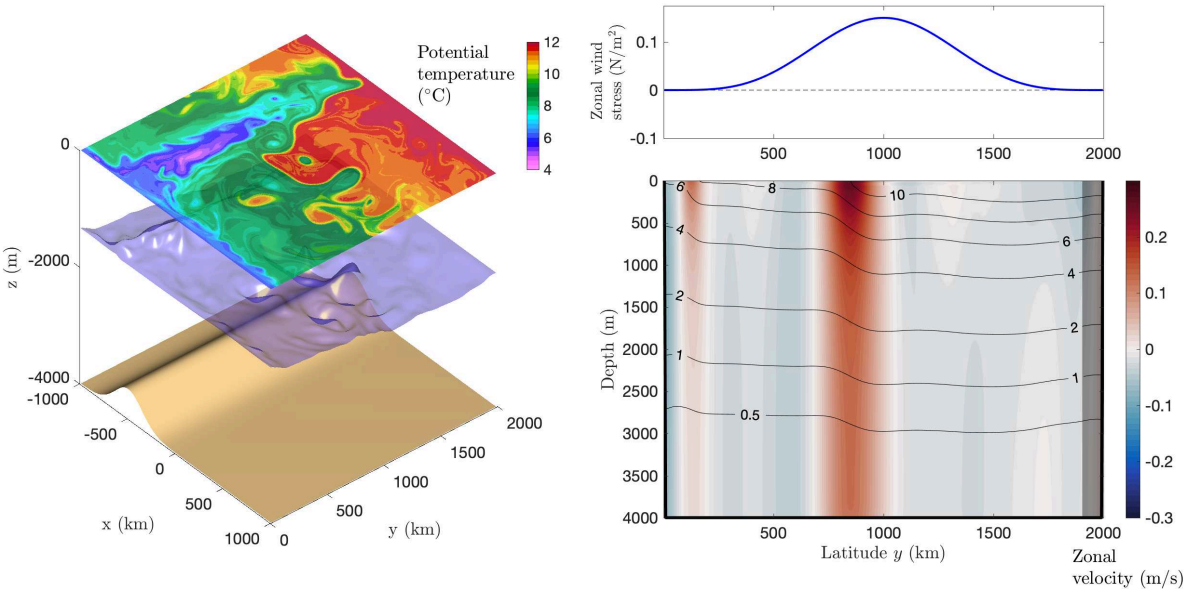

FIG. A12. Illustration of our MIT general circulation model (MITgcm, Marshall et al. 1997a,b) configuration. (Left) Model bathymetry (brown), a snapshot of the 2°C isotherm (blue), and a snapshot of the sea surface temperature (color scale). (Top-right) Latitudinal profile of zonal wind stress applied at the model surface. (Bottom-right) Zonal velocity (colors) and potential temperature (black contours), averaged zonally and temporally over 20 years in statistically steady state. The sponge layer at the northern boundary is represented as gray.

between the establishment of topographic form stress in prograde and retrograde channel flows (Fig. A13), and the associated asymmetry in the zonal transport. Our standing wave theory reproduces the topographic form stress ratio $R_{\rm TFS}$ in the MITgcm experiments (Fig. A14) more closely than in the isopycnal model experiments, and this agreement is less strongly influenced by the inclusion of an eddy viscosity. Note that for retrograde flows, the zonal-mean barotropic flow predicted by the standing wave theory is symmetric, whereas in the MITgcm experiments the barotropic flow becomes concentrated in an asymmetric jet (see Fig. A12). This asymmetry is likely introduced by a combination of the imposed exponential northern stratification and the northward excursion of barotropic potential vorticity contours over the ridge, combined with eddy-mean flow interaction in the jet (Youngs et al. 2017). We conclude that the central findings of this study extend to general circulation models, at least in the idealized channel geometry used here.

APPENDIX B

Standing Wave Theory With Transient Eddy Viscosity

In this Appendix we extend our standing wave theory (Section 4) to include an eddy viscosity. We take a time average of the quasigeostrophic potential vorticity equation (13a) to obtain, after some manipulations,

$$\overline{q}^t{}_t + J(\overline{\psi}^t, \overline{q}^t) = -\nabla\cdot\overline{\mathbf{u}^* q^*}^t - \frac{1}{\rho_0 H}\frac{\partial\tau}{\partial y} - \frac{r_b}{H}\overline{\zeta}^t. \qquad \text{(B1)}$$

Here $\overline{\bullet}^t$ denotes a time-mean and $\bullet^* = \bullet - \overline{\bullet}^t$ denotes deviations from the time-mean. We then assume that the transient eddy potential vorticity flux serves to destroy time-mean enstrophy, *i.e.*

$$\overline{\mathbf{u}^* q^*}^t = -\nu\nabla\overline{\zeta}^t. \qquad \text{(B2)}$$

We then substitute (B2) into (B1), dropping the $\overline{\bullet}^t$ notation for time-mean quantities, to obtain

$$q_t + J(\psi, q) = \nu\nabla^2\zeta - \frac{1}{\rho_0 H}\frac{\partial\tau}{\partial y} - \frac{r_b}{H}\zeta. \qquad \text{(B3)}$$

This equation is identical to (13a), with the exception of the additional eddy viscosity term on the right-hand side.

We solve (B3) following the steps detailed in Sec. 4. This leads to a modified solution for the Fourier modes of the standing wave streamfunction (B4),

$$\hat{\psi}_k = \frac{f_0}{k^2}\frac{U\left[(Uk^2 + c_k) + i\left(\frac{r_b}{Hk} + \nu k\right)\right]}{(U + c_k)^2 + \left(\frac{r_b}{kH} + \nu k\right)^2}\frac{(\hat{\eta}_b)_k}{H}. \qquad \text{(B4)}$$

Similarly, we obtain the following expression for the topographic form stress,

$$f_0\overline{\psi'_x\eta'_b} = -\frac{1}{2}\sum_k \frac{(\hat{\eta}_b)_k^2}{H^2}\cdot\frac{U f_0^2\left(r_b + H\nu k^2\right)/k^2}{(U + c_k)^2 + \left(\frac{r_b}{Hk} + \nu k\right)^2}. \qquad \text{(B5)}$$

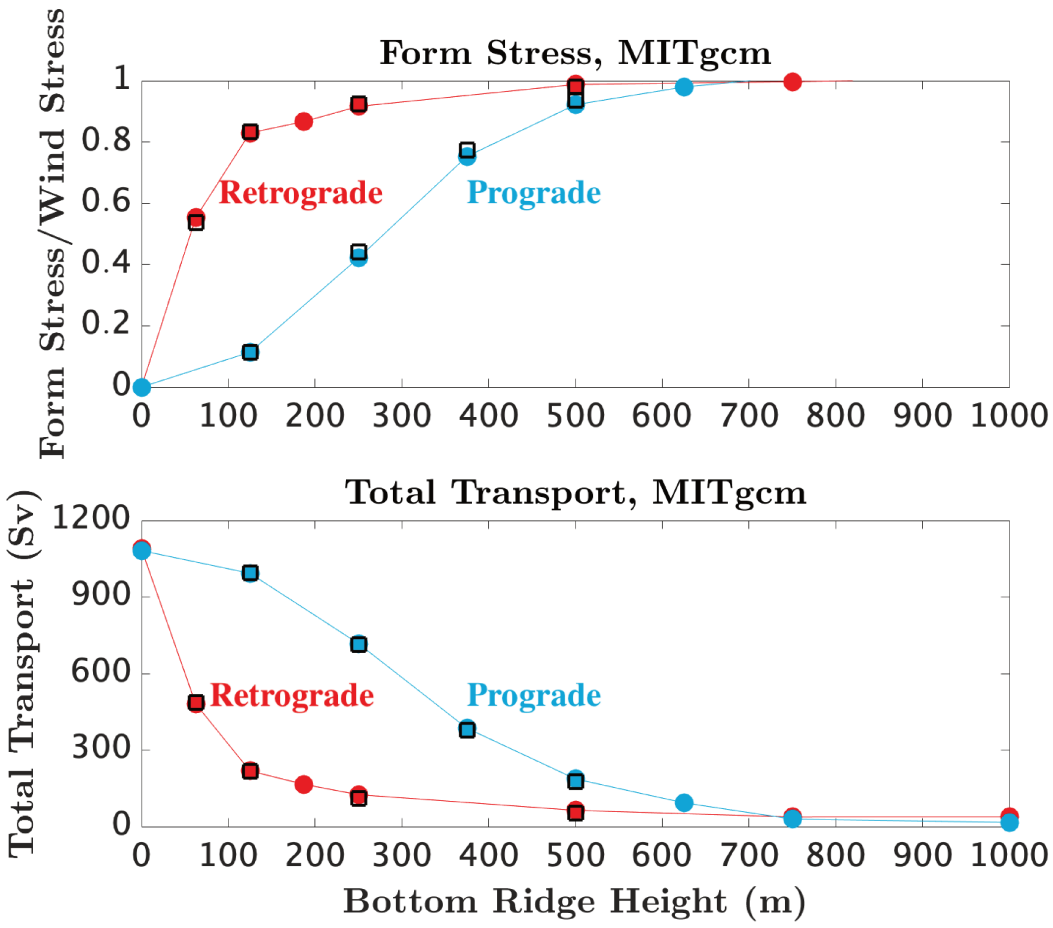

FIG. A13. As Fig. 4, but diagnostics drawn from our MIT general circulation model (MITgcm Marshall et al. 1997a,b) simulations. Points with and without black borders correspond to high-resolution (6.25 km grid spacing) and low-resolution (12.5 km grid spacing) simulations, respectively.

Note that these equations are structurally similar to (17) and (19), but now both bottom friction and the eddy viscosity serve to shift the phase of the standing wave from that of the bathymetry and contribute to the topographic form stress.

An alternative ansatz to (B2) is that eddy potential vorticity fluxes are directed down the mean potential vorticity gradient (*e.g.* Abernathey and Cessi 2014). This ansatz has a stronger basis in baroclinic flows, in which the eddy potential vorticity fluxes to residual transports along isopycnal layers (*e.g.* Marshall and Radko 2003; Marshall and Speer 2012), but its applicability to the barotropic flow is less clear. We therefore opt for (B2) because it serves to regularize the retrograde standing wave solutions without qualitatively changing the conclusions drawn from the theory. A more comprehensive treatment of the role of transient eddies in establishing topographic form stress is left for future work.

References

Abernathey, R., and P. Cessi, 2014: Topographic enhancement of eddy efficiency in baroclinic equilibration. *J. Phys. Oceanogr.*, **44**, 2107–2126.

Abernathey, R., J. Marshall, and D. Ferreira, 2011: The Dependence of Southern Ocean Meridional Overturning on Wind Stress. *J. Phys. Oceanogr.*, **41**, 2261–2278.

Arakawa, A., and V. R. Lamb, 1981: A potential enstrophy and energy conserving scheme for the shallow water equations. *Monthly Weather Review*, **109 (1)**, 18–36.

Arnol'd, V. I., 1966: An a priori estimate in the theory of hydrodynamic stability. *Izv. Vyssh. Uchebn. Zaved. Mat.*, **54**, 3 – 5.

Bischoff, T., and A. F. Thompson, 2014: Configuration of a Southern Ocean storm track. *J. Phys. Oceanogr.*, **44 (12)**, 3072–3078.

Brearley, J. A., R. S. Pickart, H. Valdimarsson, S. Jonsson, R. W. Schmitt, and T. W. N. Haine, 2012: The East Greenland boundary current system south of Denmark Strait. *Deep Sea Res. Pt. 1*, **63**, 1–19.

Brink, K. H., 1986: Topographic drag due to barotropic flow over the continental shelf and slope. *J. Phys. Oceanogr.*, **16 (12)**, 2150–2158.

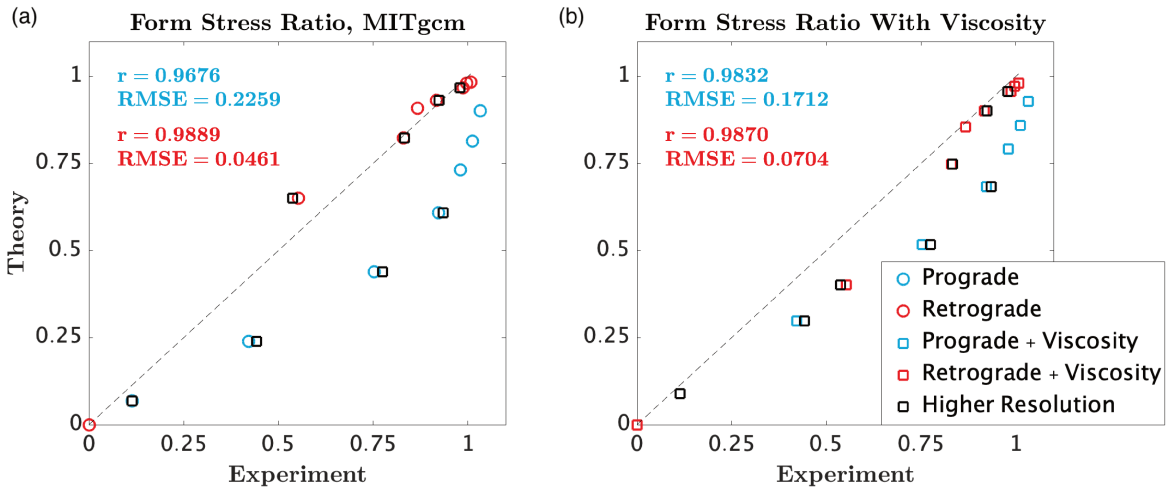

FIG. A14. As Fig. 8, but diagnostics drawn from our MIT general circulation model (MITgcm Marshall et al. 1997a,b) simulations. Additional black symbols have been added to indicate experiments run at higher horizontal resolution (see Appendix A).

Chelton, D. B., R. A. De Szoeke, M. G. Schlax, K. El Naggar, and N. Siwertz, 1998: Geographical variability of the first baroclinic Rossby radius of deformation. *J. Phys. Oceanogr.*, **28 (3)**, 433–460.

Constantinou, N. C., and W. R. Young, 2017: Beta-plane turbulence above monoscale topography. *J. Fluid Mech.*, **827**, 415–447.

Davey, M. K., 1980: A quasi-linear theory for rotating flow over topography. part 1. steady β-plane channel. *J. Fluid Mech.*, **99 (02)**, 267–292.

Donohue, K. A., K. L. Tracey, D. R. Watts, M. P. Chidichimo, and T. K. Chereskin, 2016: Mean Antarctic Circumpolar Current transport measured in Drake Passage. *Geophys. Res. Lett.*, **43 (22)**, 11–760.

Durran, D. R., 1991: The third-order Adams-Bashforth method: An attractive alternative to leapfrog time differencing. *Mon. Weather Rev.*, **119 (3)**, 702–720.

Gascard, J.-C., G. Raisbeck, S. Sequeira, F. Yiou, and K. A. Mork, 2004: The Norwegian Atlantic Current in the Lofoten basin inferred from hydrological and tracer data (129I) and its interaction with the Norwegian Coastal Current. *Geopyhs. Res. Lett.*, **31 (1)**.

Goszczko, I., R. B. Ingvaldsen, and I. H. Onarheim, 2018: Wind-driven cross-shelf exchange—West Spitsbergen current as a source of heat and salt for the adjacent shelf in Arctic winters. *J. Geophys. Res. Oceans*, **123 (4)**, 2668–2696.

Griffies, S. M., and R. W. Hallberg, 2000: Biharmonic friction with a Smagorinsky-like viscosity for use in large-scale eddy-permitting ocean models. *Monthly Weather Review*, **128 (8)**, 2935–2946.

Hallberg, R., 2013: Using a resolution function to regulate parameterizations of oceanic mesoscale eddy effects. *Ocean Modell.*, **72**, 92–103.

Hallberg, R., and A. Gnanadesikan, 2001: An exploration of the role of transient eddies in determining the transport of a zonally reentrant current. *J. Phys. Oceanogr.*, **31 (11)**, 3312–3330.

Hattermann, T., 2018: Antarctic thermocline dynamics along a narrow shelf with easterly winds. *J. Phys. Oceanogr.*, **48 (10)**, 2419–2443.

Hazel, J. E., and A. L. Stewart, 2019: Multi-Decadal Trends in Easterly Wind Stress around the Antarctic Coast. *Journal of Climate*, **32**, 1895–1918.

Hogg, A. M., 2010: An Antarctic Circumpolar Current driven by surface buoyancy forcing. *Geophys. Res. Lett.*, **37 (23)**.

Hogg, A. M., W. K. Dewar, P. Berloff, and M. L. Ward, 2011: Kelvin wave hydraulic control induced by interactions between vortices and topography. *J. Fluid Mech.*, **687**, 194.

Hogg, A. M., M. P. Meredith, D. P. Chambers, E. P. Abrahamsen, C. W. Hughes, and A. K. Morrison, 2015: Recent trends in the southern ocean eddy field. *Journal of Geophysical Research: Oceans*, **120 (1)**, 257–267.

Hogg, A. M. C., M. P. Meredith, J. R. Blundell, and C. Wilson, 2008: Eddy heat flux in the Southern Ocean: response to variable wind forcing. *J. Climate*, **21 (4)**, 608–620.

Holloway, G., K. Brink, and D. Haidvogel, 1989: Topographic stress in coastal circulation dynamics. *Poleward flows along eastern ocean boundaries*, Springer, 315–330.

Howard, E., A. McC. Hogg, S. Waterman, and D. P. Marshall, 2015: The injection of zonal momentum by buoyancy forcing in a Southern Ocean model. *J. Phys. Oceanogr.*, **45 (1)**, 259–271.

Hughes, C. W., 1997: Comments on "On the obscurantist physics of 'form drag' in theorizing about the circumpolar current". *J. Phys. Oceanogr.*, **27 (1)**, 209–210.

Jacobs, S. S., 1991: On the nature and significance of the Antarctic Slope Front. *Mar. Chem.*, **35 (1)**, 9–24.

Jansen, M. F., I. M. Held, A. Adcroft, and R. Hallberg, 2015: Energy budget-based backscatter in an eddy permitting primitive equation model. *Ocean Modelling*, **94**, 15 – 26.

Johnson, G. C., and H. L. Bryden, 1989: On the size of the antarctic circumpolar current. *Deep Sea Research Part A. Oceanographic Research Papers*, **36 (1)**, 39 – 53.

Langlais, C. E., A. Lenton, R. Matear, D. Monselesan, B. Legresy, E. Cougnon, and S. Rintoul, 2017: Stationary rossby waves dominate

subduction of anthropogenic carbon in the southern ocean. *Sci. Rep.*, **7 (1)**, 1–10.

Large, W. G., J. C. McWilliams, and S. C. Doney, 1994: Oceanic vertical mixing: A review and a model with a nonlocal boundary layer parameterization. *Rev. Geophys.*, **32 (4)**, 363–404.

Large, W. G., and S. G. Yeager, 2009: The global climatology of an interannually varying air–sea flux data set. *Climate Dynam.*, **33 (2)**, 341–364.

Lin, X., X. Zhai, Z. Wang, and D. R. Munday, 2018: Mean, Variability, and Trend of Southern Ocean Wind Stress: Role of Wind Fluctuations. *Journal of Climate*, **31 (9)**, 3557–3573.

Liu, G., Y. He, H. Shen, and J. Guo, 2011: Global drag-coefficient estimates from scatterometer wind and wave steepness. *IEEE Transactions on Geoscience and Remote Sensing*, **49 (5)**, 1499–1503.

Manucharyan, G. E., and P. E. Isachsen, 2019: Critical role of continental slopes in halocline and eddy dynamics of the Ekman-driven Beaufort Gyre. *J. Geophys. Res. Oceans*, **124 (4)**, 2679–2696.

Marshall, D., 1995: Topographic steering of the Antarctic Circumpolar Current. *J. Phys. Oceanogr.*, **25 (7)**, 1636–1650.

Marshall, D. P., 2016: A theoretical model of long Rossby waves in the Southern Ocean and their interaction with bottom topography. *Fluids*, **1 (2)**, 17.

Marshall, D. P., M. H. P. Ambaum, J. R. Maddison, D. R. Munday, and L. Novak, 2017: Eddy saturation and frictional control of the Antarctic Circumpolar Current. *Geophys. Res. Lett.*, **44 (1)**, 286–292.

Marshall, G. J., 2003: Trends in the Southern Annular Mode from observations and reanalyses. *J. Climate*, **16 (24)**, 4134–4143.

Marshall, J., A. Adcroft, C. Hill, L. Perelman, and C. Heisey, 1997a: A finite-volume, incompressible Navier Stokes model for studies of the ocean on parallel computers. *J. Geophys. Res. Oceans*, **102**, 5753–5766.

Marshall, J., C. Hill, L. Perelman, and A. Adcroft, 1997b: Hydrostatic, quasi-hydrostatic, and nonhydrostatic ocean modeling. *J. Geophys. Res. Oceans*, **102**, 5733–5752.

Marshall, J., and T. Radko, 2003: Residual-mean solutions for the Antarctic Circumpolar Current and its associated overturning circulation. *J. Phys. Oceanogr.*, **33 (11)**, 2341–2354.

Marshall, J., and K. Speer, 2012: Closure of the meridional overturning circulation through Southern Ocean upwelling. *Nature Geosci.*, **5 (3)**, 171–180.

Masich, J., T. K. Chereskin, and M. R. Mazloff, 2015: Topographic form stress in the Southern Ocean state estimate. *J. Geophys. Res. Oceans*, **120 (12)**, 7919–7933.

Masich, J., M. R. Mazloff, and T. K. Chereskin, 2018: Interfacial form stress in the Southern Ocean state estimate. *J. Geophys. Res. Oceans*, **123 (5)**, 3368–3385.

Mazloff, M. R., P. Heimbach, and C. Wunsch, 2010: An eddy-permitting Southern Ocean state estimate. *J. Phys. Oceanogr.*, **40 (5)**, 880–899.

Meneghello, G., J. Marshall, J.-M. Campin, E. Doddridge, and M.-L. Timmermans, 2018: The ice-ocean governor: Ice-ocean stress feedback limits Beaufort Gyre spin-up. *Geophys. Res. Lett.*, **45 (20)**, 11–293.

Meredith, M. P., 2016: Understanding the structure of changes in the Southern Ocean eddy field. *Geophys. Res. Lett.*, **43 (11)**, 5829–5832.

Morrison, A. K., and A. M. Hogg, 2013: On the relationship between Southern Ocean overturning and ACC transport. *J. Phys. Oceanogr.*, **43 (1)**, 140–148.

Munday, D. R., H. L. Johnson, and D. P. Marshall, 2013: Eddy saturation of equilibrated circumpolar currents. *J. Phys. Oceanogr.*, **43 (3)**, 507–532.

Munk, W. H., and E. Palmén, 1951: Note on the dynamics of the Antarctic Circumpolar Current. *Tellus*, **3 (1)**, 53–55.

Myers, P. G., C. Donnelly, and M. H. Ribergaard, 2009: Structure and variability of the West Greenland Current in summer derived from 6 repeat standard sections. *Prog. Oceanogr.*, **80 (1-2)**, 93–112.

Nadeau, L.-P., and R. Ferrari, 2015: The Role of Closed Gyres in Setting the Zonal Transport of the Antarctic Circumpolar Current. *Journal of Physical Oceanography*, **45 (6)**, 1491–1509.

Naveira Garabato, A. C., A. J. G. Nurser, R. B. Scott, and J. A. Goff, 2013: The impact of small-scale topography on the dynamical balance of the ocean. *Journal of Physical Oceanography*, **43 (3)**, 647 – 668.

Olbers, D., 1998: Comments on "On the obscurantist physics of 'form drag'in theorizing about the Circumpolar Current. *J. Phys. Oceanogr.*, **28 (8)**, 1647–1654.

Olbers, D., D. Borowski, C. Völker, and J.-O. Wolff, 2004: The dynamical balance, transport and circulation of the Antarctic Circumpolar Current. *Antarct. Sci.*, **16 (4)**, 439–470.

Patmore, R. D., P. R. Holland, D. R. Munday, A. C. Naveira Garabato, D. P. Stevens, and M. P. Meredith, 2019: Topographic Control of Southern Ocean Gyres and the Antarctic Circumpolar Current: A Barotropic Perspective. *J. Phys. Oceanogr.*, **49 (12)**, 3221–3244.

Pedlosky, J., 1987: *Geophysical fluid dynamics*. Springer.

Pinardi, N., A. Rosati, and R. Pacanowski, 1995: The sea surface pressure formulation of rigid lid models. implications for altimetric data assimilation studies. *Journal of Marine Systems*, **6 (1)**, 109 – 119.

Pringle, J. M., 2002: Enhancement of wind-driven upwelling and downwelling by alongshore bathymetric variability. *J. Phys. Oceanogr.*, **32 (11)**, 3101–3112.

Robertson, R., L. Padman, and G. D. Egbert, 1998: Tides in the Weddell Sea. *Ocean, ice, and atmosphere: interactions at the Antarctic Continental Margin*, 341–369.

Schulze Chretien, L. M., and E. Frajka-Williams, 2018: Wind-driven transport of fresh shelf water into the upper 30m of the Labrador Sea. *Ocean Sci.*, **14 (5)**, 1247–1264.

Smagorinsky, J., 1963: General circulation experiments with the primitive equations: I. The basic experiment. *Mon. Weather Rev.*, **91 (3)**, 99–164.

Solodoch, A., A. L. Stewart, and J. C. McWilliams, 2021: Formation of anticyclones above topographic depressions. *Journal of Physical Oceanography*, **51**, 207–228.

Spall, M. A., 2004: Boundary Currents and Watermass Transformation in Marginal Seas. *J. Phys. Oceanogr.*, **34 (5)**, 1197–1213.

Spall, M. A., and L. N. Thomas, 2016: Downfront winds over buoyant coastal plumes. *J. Phys. Oceanogr.*, **46 (10)**, 3139–3154.

Stanley, G. J., T. E. Dowling, M. E. Bradley, and D. P. Marshall, 2020: Ertel potential vorticity versus bernoulli potential on approximately neutral surfaces in the antarctic circumpolar current. *Journal of Physical Oceanography*, **50 (9)**, 2621 – 2648.

Stevens, D. P., and V. O. Ivchenko, 1997: The zonal momentum balance in an eddy-resolving general-circulation model of the Southern Ocean. *Quart. J. Roy. Meteor. Soc.*, **123**, 929–952.

Stewart, A. L., 2019: Approximating isoneutral ocean transport via the Temporal Residual Mean. *Fluids*, **4**, 179.

Stewart, A. L., and P. J. Dellar, 2016: An energy and potential enstrophy conserving numerical scheme for the multi-layer shallow water equations with complete Coriolis force. *Journal of Computational Physics*, **313**, 99–120.

Stewart, A. L., and A. M. Hogg, 2017: Reshaping the Antarctic Circumpolar Current via Antarctic Bottom Water Export. *J. Phys. Oceanogr.*, **47 (10)**, 2577–2601.

Stewart, A. L., A. Klocker, and D. Menemenlis, 2018: Circum-antarctic shoreward heat transport derived from an eddy- and tide-resolving simulation. *Geophysical Research Letters*, **45 (2)**, 834–845.

Stewart, A. L., A. Klocker, and D. Menemenlis, 2019: Acceleration and overturning of the Antarctic Slope Current by winds, eddies, and tides. *Journal of Physical Oceanography*, **43**, 2043–2074.

Stewart, A. L., and A. F. Thompson, 2012: Sensitivity of the ocean's deep overturning circulation to easterly Antarctic winds. *Geophys. Res. Lett.*, **39 (18)**, L18 604.

Stewart, A. L., and A. F. Thompson, 2013: Connecting Antarctic Cross-Slope Exchange with Southern Ocean Overturning. *J. Phys. Oceanogr.*, **43**, 1453–1471.

Stewart, A. L., and A. F. Thompson, 2015a: Eddy-mediated transport of warm Circumpolar Deep Water across the Antarctic Shelf Break. *Geophys. Res. Lett.*, **42**, 432–440.

Stewart, A. L., and A. F. Thompson, 2015b: The Neutral Density Temporal Residual Mean overturning circulation. *Ocean Modelling*, **90**, 44–56.

Stewart, A. L., and A. F. Thompson, 2016: Eddy generation and jet formation on the Antarctic continental slope. *J. Phys. Oceanogr.*, **46**, 3729–3750.

Straub, D. N., 1993: On the transport and angular momentum balance of channel models of the antarctic circumpolar current. *Journal of Physical Oceanography*, **23 (4)**, 776 – 782.

Talley, L. D., 2013: Closure of the global overturning circulation through the Indian, Pacific, and Southern Oceans: Schematics and transports. *Oceanography*, **26 (1)**, 80–97.

Thompson, A. F., 2008: The atmospheric ocean: eddies and jets in the Antarctic Circumpolar Current. *Phil. Trans. Roy. Soc. A*, **366 (1885)**, 4529–4541.

Thompson, A. F., and A. C. Naveira Garabato, 2014: Equilibration of the Antarctic Circumpolar Current by standing meanders. *J. Phys. Oceanogr.*, **44 (7)**, 1811–1828.

Thompson, A. F., A. L. Stewart, and T. Bischoff, 2016: A multi-basin residual-mean model for the global overturning circulation. *Journal of Physical Oceanography*, **46**, 2583–2604.

Thompson, A. F., A. L. Stewart, P. Spence, and K. J. Heywood, 2018: The Antarctic Slope Front in a Changing Climate. *Reviews of Geophysics*, **56**, 741–770.

Towns, J., and Coauthors, 2014: XSEDE: Accelerating scientific discovery. *Computing in Science Engineering*, **16 (5)**, 62–74, doi: 10.1109/MCSE.2014.80.

Tréguier, A.-M., and J. C. McWilliams, 1990: Topographic influences on wind-driven, stratified flow in a β-plane channel: An idealized model for the Antarctic Circumpolar Current. *J. Phys. Oceanogr.*, **20 (3)**, 321–343.

Vallis, G. K., 2006: *Atmospheric and oceanic fluid dynamics: fundamentals and large-scale circulation*. Cambridge Univ Pr.

Vallis, G. K., and M. E. Maltrud, 1993: Generation of mean flows and jets on a beta plane and over topography. *J. Phys. Oceanogr.*, **23 (7)**, 1346–1362.

Wang, Y., and A. L. Stewart, 2018: Eddy dynamics over continental slopes under retrograde winds: Insights from a model intercomparison. *Ocean Modell.*, **121**, 1–18.

Wang, Y., and A. L. Stewart, 2020: Scalings for eddy buoyancy transfer across continental slopes under retrograde winds. *Ocean Modell.*, **147**, 101 579.

Ward, M. L., and A. M. Hogg, 2011: Establishment of momentum balance by form stress in a wind-driven channel. *Ocean Modell.*, **40 (2)**, 133–146.

Warren, B. A., J. H. LaCasce, and P. E. Robbins, 1996: On the obscurantist physics of "form drag" in theorizing about the Circumpolar Current. *J. Phys. Oceanogr.*, **26 (10)**, 2297–2301.

Yang, L., M. Nikurashin, A. M. Hogg, and B. M. Sloyan, 2018: Energy loss from transient eddies due to lee wave generation in the Southern Ocean. *J. Phys. Oceanogr.*, **48 (12)**, 2867–2885.

Youngs, M. K., A. F. Thompson, A. Lazar, and K. J. Richards, 2017: Acc meanders, energy transfer, and mixed barotropic–baroclinic instability. *J. Phys. Oceanogr.*, **47 (6)**, 1291–1305.

Zhao, K. X., A. L. Stewart, and J. C. McWilliams, 2019: Sill-influenced exchange flows in ice shelf cavities. *J. Phys. Oceanogr.*, **49 (1)**, 163–191.